University of Central Florida
STARS

Electronic Theses and Dissertations

2017

Quantification of Non-stoichiometry and Impurities in Transparent YAG Ceramics by Laser-induced Breakdown Spectroscopy (LIBS)

Sudeep Pandey
University of Central Florida

 Part of the Physics Commons
Find similar works at: https://stars.library.ucf.edu/etd
University of Central Florida Libraries http://library.ucf.edu

This Doctoral Dissertation (Open Access) is brought to you for free and open access by STARS. It has been accepted for inclusion in Electronic Theses and Dissertations by an authorized administrator of STARS. For more information, please contact STARS@ucf.edu.

STARS Citation
Pandey, Sudeep, "Quantification of Non-stoichiometry and Impurities in Transparent YAG Ceramics by Laser-induced Breakdown Spectroscopy (LIBS)" (2017). *Electronic Theses and Dissertations*. 5581.
https://stars.library.ucf.edu/etd/5581

QUANTIFICATION OF NON-STOICHIOMETRY AND IMPURITIES IN TRANSPARENT YAG CERAMICS BY LASER-INDUCED BREAKDOWN SPECTROSCOPY

by

SUDEEP J. PANDEY

B.Sc., Tribhuvan University, 2006
M.Sc., Tribhuvan University, 2010
M.S., University of Central Florida, 2013

A dissertation submitted in partial fulfillment of the requirements
for the degree of Doctor of Philosophy
in the Department of Physics
in the College of Sciences
at the University of Central Florida
Orlando, Florida

Summer Term
2017

Major Professor: Romain Gaume

© 2017 Sudeep J. Pandey

ABSTRACT

Transparent ceramics are an important class of optical materials with applications in street-lighting, high-strength windows, electro- and magneto-optical isolators, high-power laser gain media and nuclear radiation detectors. Compared to single-crystal growth, ceramic processing enables size scalability, near net-shape forming and prevents issues associated with dopant segregation and inhomogeneity, such as stress-induced birefringence and wavefront distortions. The fabrication of high optical grade ceramics by route of powder sintering, relies on a controlled set of techniques preventing the formation of scattering centers (pores and secondary phases) and harmful point defects (color centers, charge-carrier trapping sites). This thesis work investigates a novel approach in assisting the fabrication of yttrium aluminum garnet (YAG, $Y_3Al_5O_{12}$) transparent ceramics, an important laser material, and minimizing the presence of these defects. As a line compound in the Al_2O_3-Y_2O_3 phase diagram, YAG has little tolerance for excess of either yttrium or aluminum oxides. What is more, the estimated compositional range of the garnet phase, $(5/3-0.03)<Al/Y<(5/3+0.008)$, which is at the root of fabrication inconsistencies, challenges the sensitivity of most analytical techniques. We have evaluated the use of laser-induced breakdown spectroscopy (LIBS), a rapid, cost effective, non-destructive, and versatile technique, in the determination of stoichiometry and impurities at the various stages of the ceramic fabrication, i.e. in powders, green and sintered bodies. It was found that enough sensitivity and accuracy can be achieved on a custom-built system to discern 0.3 mole percent in the Al/Y ratio. To understand the influence of the plasma temperature on the ratio of the atomic emission lines of Al and Y species, simulations of YAG-based laser-induced plasmas were performed. The results have guided our experimental protocol by showing that above 12000 K, the Al/Y intensity ratio and thus the

sensitivity of the measurement increases sharply with plasma temperature. In addition, we show that LIBS can be used to monitor the concentrations of unintentional trace impurities along those of sintering additives (SiO_2) customarily used for the removal of porosity during firing. Hence, we reveal, for example, that less than 30% of SiO_2 remains in the final ceramic due to evaporation during high temperature sintering.

This work not only extends the range of capabilities of LIBS by showing how highly sensitive quantification of major elements can be performed in insulating materials, but also provides a new set of tools for estimating the range of solid-state solutions in advanced materials and understanding the densification of ceramics. We foresee that such capability will be invaluable for quality control purposes and in areas where fine and reproducible compositional tuning (defect engineering) is needed.

To my wife Mona and my parents

ACKNOWLEDGMENTS

First and foremost, I would like to express my sincerely gratitude to my advisor Dr. Romain Gaume. This work is made possible only because of his constant guidance, support and motivation. The countless hours he spent with me discussing various problems and sharing his deep knowledge has had a great influence on the development of my intellectual abilities. I would like to thank Dr Matthieu Baudelet for showing me the different facets of the LIBS technique and introducing me to this vibrant community. I am very grateful to Dr. Vincent Motto-Ros and Dr Mauro Martinez for helping me with some of the experiments. I would like to thank my colleagues Taylor Shoulders, Xuan Chen, Matthew Julian and Richard Lock for their companionship. Last but not the least, I would like to thank my wife Mona for here never ending support and undiminishing faith in me.

TABLE OF CONTENTS

LIST OF FIGURES xi
LIST OF TABLES xvi
LIST OF ABBREVIATIONS xvii
CHAPTER ONE: INTRODUCTION 1
1.1 Transparent Optical Ceramics 1
1.2 Yttrium aluminum garnet (YAG) 3
1.2.1 Nonreactive sintering 5
1.2.2 Reactive sintering 5
1.3 Factors affecting the optical properties of YAG TOCs 6
1.3.1 Point defects and secondary phase precipitation caused by non-stoichiometry 6
1.3.2 Residual pores 10
1.3.3 Impurities 10
1.4 Previous studies on the quantification of non-stoichiometry and impurities in YAG 13
1.5 LIBS as an analytical tool for the quantification of non-stoichiometry and impurities 15
1.6 Summary and dissertation outline 15
CHAPTER TWO: ATOMIC EMISSION SPECTROSCOPY AND LIBS 18
2.1 Fundamentals of atomic emission spectroscopy 18
2.1.1 Line broadening 21
2.1.1.1 Natural line broadening 21
2.1.1.2 Doppler broadening 21

2.1.1.3 Stark broadening 22

2.1.1.4 Convolution of line broadening 22

2.1.2 Self-absorption 24

2.2 Laser-induced breakdown spectroscopy 25

2.2.1 Laser ablation and plasma formation 25

2.2.2 Characteristics of a LIBS plasma 30

2.3 Components of LIBS system 32

2.3.1 Laser 32

2.3.2 Focusing Optics and plasma light collection 33

2.3.3 Spectrometer 34

2.3.4 Device for recording the spectra 35

2.3.4.1 Wavelength calibration 36

2.3.4.2 Spectral response calibration 36

2.4 Quantitative elemental analysis by LIBS 37

2.5 Factors affecting the quantitative elemental analysis by LIBS 38

2.5.1 Laser irradiance on the sample surface 38

2.5.2 ICCD timings 40

2.5.3 Choice of emission lines 40

2.5.4 Ambient conditions 40

2.5.5 Matrix effects 41

2.6 Internal standardization 41

CHAPTER THREE: SIMULATIO OF YAG PLASMA FORMED IN AIR 43

3.1 Calculations 45

3.2 Results and discussion 49

3.3 Conclusion 55

CHAPTER FOUR: QUANTIFICATION OF NONSTOICHIOMERY IN YAG 56

4.1 Fabrication of ceramics with varied compositions near the garnet phase 56

4.2 LIBS analysis for the quantification of stoichiometry 59

4.3 Results and discussion 62

CHAPTER FIVE: STUDY OF THE EFFECT OF POWDER COMPACT DENSITY ON LIBS ANALYSIS OF MINOR ELEMENT 65

5.1 Sample preparation 65

5.2 LIBS protocol 67

5.3 Results and discussion 67

5.4 Conclusion 74

CHAPTER SIX: QUANTIFICATION OF SIO_2 SINTERING ADDITIVE IN YAG 76

6.1 Sample preparation 77

6.2 Fabrication of calibration samples 77

6.3 LIBS system and experimental protocol 78

6.4 Results and discussion 79

6.5 Conclusion 83
CHAPTER SEVEN: CONCLUSION & PROSPECTS 85
APPENDIX A: QUANTIFICATION OF NONSTOICHIOMETRY IN YAG BY ICP-AES 88
APPENDIX B: PUBLICATIONS 91
B.1 Journal publications 92
B.2 Conferences 92
LIST OF REFERENCES 93

LIST OF FIGURES

Figure 1. Transparent YAG fabricated in our lab. Right Ce:YAG and left Tm:YAG 3

Figure 2. Crystal structure of YAG..... 4

Figure 3. Y_2O_3-Al_2O_3 phase diagram. Inset (a) 2 mol % excess yttria which causes the precipitation of YAP at the grain boundary. (b) Stoichiometric YAG with clean grain boundary 8

Figure 4. Effect of SiO_2 sintering aid on the densification of YAG ceramics: (a) abnormal grain growth and closed pores due to the lack of sintering aid (b) uniform grain growth with virtually non-existent porosity because of SiO_2 addition yielding a transparent sample. 12

Figure 5. Variation of YAG lattice parameter with non-stoichiometry. 14

Figure 6. Variation of terahertz spectrum of YAG with non-stoichiometry..... 14

Figure 7. Temporal evolution of LIBS plasma in aluminum oxide pellet. The laser energy and gate width was set at 8 mJ and 50 ns respectively..... 31

Figure 8. Schematics of a typical LIBS setup. The laser shown here is a 1064 nm Q-switched Nd:YAG. M is a dichroic mirror that is highly reflective above 1000 nm. L1 is the lens to focus laser on the sample surface. L2 and L4 are lenses to focus plasma light into CCD camera C2 and C1 respectively. Lens L3 focuses plasma light into the spectrometer..... 32

Figure 9. Hypothetical calibration curve to find the Al/Y molar ratio in YAG samples..... 43

Figure 10. Algorithm flowchart for calculating number densities of different species in a plasma at local thermodynamic equilibrium. (a) Iteration loop to calculate ionization equilibrium and (b) chemical equilibrium. 47

Figure 11. Number densities of plasma species as a function of temperature computed for aluminum. Circles are the simulation by Hermann *et al* [99] and the solid lines are our result. The number density of each species was normalized by the sum $n_{vap}+ n_{gas}$. 50

Figure 12. Simulation of aluminum plasma in nitrogen background. Circles are the results from [99] and the solid lines are our result. 50

Figure 13. Simulation of YAG plasma in air. The number density of ablated YAG molecules was estimated to be 1.71×10^{23} m^{-3} based on the experimentally observed crater size. The air pressure was set to 1.01×10^{5} Pa and the ratio of nitrogen to oxygen atoms was set to 3.7 to simulate the atmospheric condition. 52

Figure 14. Simulated Al/Y intensity ratio as function of plasma temperature. Al 281.61 nm and Y 278.52 nm peaks were used for this purpose. 53

Figure 15. Sensitivities of the simulated calibration curves. The results show that the sensitivity increases sharply after 14000 K. 54

Figure 16. Optical microscopy images of YAG samples. (a) Al/Y molar ratio=1.673. The bright spots are due to light scattering from Al_2O_3 precipitates (b) Transparent sample with Al/Y molar ratio=1.667 (stoichiometric YAG) and (c) Translucent sample with Al/Y molar ratio=1.6213 57

Figure 17. Flowchart depicting the fabrication process of YAG ceramics..... 58

Figure 18. Ceramic samples after vacuum sintering. Each sample is ¼" in diameter. YAG powder was laid at the bottom of the tungsten crucible to prevent sticking. Note the reddish-brown color of alumina-rich samples. The color goes away after annealing. At this stage of the process, the roughness of the surface prevents seeing the actual transparency of the samples..... 58

Figure 19. Configuration of LIBS system used in this study..... 59

Figure 20. Typical LIBS spectrum of an yttrium aluminum oxide sample, showing the Al^{+} and Y^{+} lines used for quantitative analysis. The other spectral features correspond to transitions in neutral and ionized Al and Y species..... 61

Figure 21. Variation of the 281.61 nm aluminum and 278.52 nm yttrium line intensity ratios with sample composition. The arrow points to the sample with the stoichiometric garnet phase composition (YAG). The 3 domains (labeled group I, II and III) correspond to the visible appearance of the samples: transparent for group II and translucent for groups I and III. The changes in slope, *m*, seen in the calibration curves between these groups reflect differences in laser-sample interaction. 63

Figure 22. SEM images of alumina powders used in this study. The inset is the image taken at higher magnification and hydrodynamic size distribution. (a) Sample S1 (b) Sample S2 (c) Sample S3. 66

Figure 23. LIBS spectrum of nickel spiked alumina samples in between the wavelength limit 298 nm-307nm. 68

Figure 24. Calibration curve for different laser energies for pressed pellet of powder S1. 69

Figure 25. Comparison of spectra from S1, S2 and S3. Intensity from S3 is an order of magnitude higher than both S1 and S2 powders and pressed pellets. 70

Figure 26. Simulated intensities of Al 305.47 nm, Al 305.71 nm, Ni 305.43 nm and Ni 305.76 nm peaks as a function of temperature. 71

Figure 27. (a) Boltzmann plot for S3 (b) Variation of the excitation temperature of aluminum for various powder-compacts. 72

Figure 28. Calibration curve as a function of powder compaction and particle size. Large fluctuation in signal is observed at lower densities 73

Figure 29. Variation of sensitivity with powder compaction. The numbers on top of the data points are the relative standard deviation values. 74

Figure 30. Flow chart for the fabrication of rare-earth (RE) doped YAG transparent ceramics. Samples for analysis were taken out at the steps marked by stars. 76

Figure 31. **(a)** Picture of an optical ceramic sample analyzed in the study. The inset shows the ablation craters left after the LIBS analysis. **(b)** Representative emission spectrum of a YAG ceramic analyzed by LIBS. In this example, the concentration of silica is 0.838 wt.%.

The grey area in the figure represents the 1-sigma standard deviation of the signal and the solid red curve is the average spectrum. 79

Figure 32. Calibration curve for the determination of SiO_2 concentration in YAG ceramics. The standard deviation of the blank sample is ±0.0017. 81

Figure 33. Evolution of the SiO_2 content in green bodies and sintered ceramics of YAG for different initial amounts of silica precursors. 83

Figure 34. ICP-AES data of YAG samples with Al/Y ratio ranging from 1.657 to 1.667. No apparent relationship between intensity and molar ratios are observed. The relative standard deviation of measurements is 10%. 90

LIST OF TABLES

Table 1. Evolution of the concentration of SiO_2 during the fabrication of a transparent YAG ceramic sample made by reactive sintering of Y_2O_3 and Al_2O_3 powders and doped with 0.5wt% TEOS. 82

LIST OF ABBREVIATIONS

A_{ji}	Transition probability of an electron in an atom from energy level j to i
CIP	Cold Isostatic Press
°C	Degree centigrade
CCD	Charge-coupled device
CW	Continuous Wave
E_D	Dissociation energy
E_{ion}	Ionization energy
E_j	Atomic energy levels
eV	Electron Volt
FWHM	Full width at half maximum
HP	Hot press
ICCD	Intensified charge-coupled device
ICP	Inductively coupled plasma
K	Kelvin
LIBS	Laser-induced breakdown spectroscopy
LOQ	Limit of quantification
LOD	Limit of detection
μs	Micro second
MS	Mass spectrometry
mg	Milligram
n_e	Electron number density

NIST	National Institute of Standard and Technology
ns	Nano-second
OES	Optical emission spectroscopy
ppm	Part per million
ρ	Density
SEM	Scanning Electron Microscope
TEOS	Tetraethoxysilane
U_a^Z	Partition function of species *a* in charge sate *Z*
XRD	X-ray diffraction
XRF	X-ray fluorescence
YAG	Yttrium aluminum garnet ($Y_3Al_5O_{12}$)

CHAPTER ONE: INTRODUCTION

1.1 Transparent Optical Ceramics

Transparent optical ceramics (TOC)[1] are an important class of optical materials with applications in street-lighting, high-strength windows, electro- and magneto-optical isolators, high-power laser gain media and nuclear radiation detectors. Compared to single-crystal growth, ceramic processing enables size scalability, near net-shape forming and prevents issues associated with dopant segregation and inhomogeneity, such as stress-induced birefringence and wavefront distortions. These materials are either made by sintering of powders at high temperatures but below their melting point, or by chemical vapor deposition (CVD). The development of transparent ceramics kick-started in the 1960s after the invention of translucent aluminum oxide used as an envelope for high-intensity, high-pressure sodium vapor lamps [1]. This invention revolutionized the street lighting industry and opened new applications and research prospects for these materials. Transparent optical ceramics are now used in a broad range of applications including transparent armor [2], infrared window for missile domes [3], electro-optical devices [4], phosphors [5], x-ray, γ-ray and neutron scintillators [6, 7] and laser gain media [8, 9].

As for any optical material, a high degree of transparency is achieved if the ceramic phase (and therefore the refractive index) is homogeneous at the scale of the wavelength of the light. For this reason, crystalline phases of cubic symmetry devoid of inclusions and pores can be turned into TOCs. Similarly, lower symmetry materials can be made transparent, as long as their grains are

[1] Ceramics are bulk polycrystalline, inorganic, and man-made nonmetallic materials

oriented along a common optical axis (textured) [10] or nanometric in size [11]. The level of ceramic transparency that one must achieve after processing depends on the application. In particular, transparent ceramics used as a laser gain-medium, such as neodymium doped yttrium aluminum garnet (Nd:YAG), are notoriously challenging to fabricate due to the fact that any scattering loss competes with the gain of the medium [12]. This requirement is even more stringent if these materials are used in high power applications [11]. Conversely, some amount of translucency may be required in lighting applications and CT-scan detectors.

As alluded to earlier, major single-crystal growth techniques rely on the growth interface defined by a solid-liquid or solid-vapor equilibrium, where the condensed phase refines itself by excluding unfit contaminants and secondary phases. This process has its pros (purer, strain-free and homogeneous crystals can eventually be obtained) but also its cons (homogeneous doping at a given concentration may be difficult, even impossible, if dopant segregation coefficients are different from unity). Standard solid-state sintering of ceramics, on the other hand, resembles more a closed system[2] in that dopant segregation and large scale mass transport are essentially inoperative. As a result, the global stoichiometry of the ceramic is set by the ratio of its initial constituents, i.e. higher and more homogeneous doping levels are possible, but the purity and composition of the ceramic are set at the start. Any initial departure from the stoichiometric composition can lead to the formation of secondary phases and deteriorate the optical quality of the ceramic: a process often referred to as *GIGO* by our computer scientist colleagues[3].

[2] This is only an approximation, as depending on the circumstances, some selective evaporation of a constituent can occur, or a liquid phase may be present. We will come back to this notion in Chapter 4.
[3] GIGO: Garbage In, Garbage out

In the next section, the difficulties pertaining to the densification and reduction of optical losses in polycrystalline YAG are discussed.

1.2 Yttrium aluminum garnet (YAG)

YAG is a synthetic garnet with formula $Y_3Al_5O_{12}$. In the crystal structure, shown in figure 5, yttrium occupies dodecahedron sites (coordination number 8), whereas aluminum occupies octahedral and tetrahedral sites (coordination number 6 and 4, respectively) [13]. It is a body centered cubic structure that contains 160 atoms per unit cell, and which can accommodate a variety of dopants by substitution. Neodymium-doped single-crystals of YAG (Nd:YAG), for example, have been used as a laser gain media since the 1960s and are still very prevalent to this day. Other rare-earth (Ce, Eu, Tb, Dy) doped YAG are also used as phosphors [14], scintillators [15] and white LEDs (WLEDs) [16].



Figure 1. Transparent YAG fabricated in our lab. Right Ce:YAG and left Tm:YAG

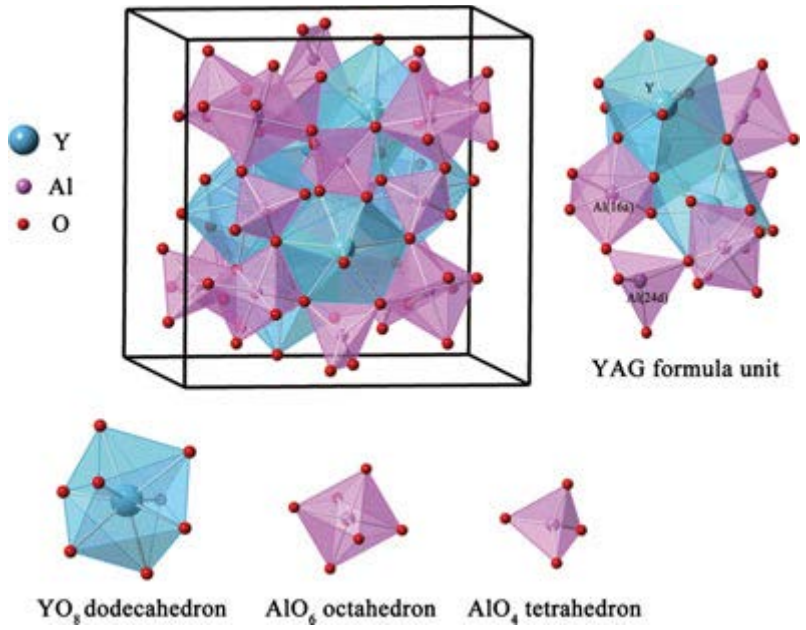


Figure 2. Crystal structure of YAG

YAG single-crystals are predominantly grown by the Czochralski method. Due to the low neodymium segregation coefficient of 0.2 in YAG, the host cannot incorporate more than 1 at% dopant [12]. Furthermore, the YAG crystal is grown by congruent melting which requires a very high temperature in excess of 2000°C and growth period exceeding 1000 hours. To make matter worse, YAG crystals grown by this technique are not homogeneous throughout the volume of the ingot, hence large slabs for high power laser application cannot be fabricated [17]. To overcome these shortcomings, attention was turned into its polycrystalline form. In addition to the relative ease of fabrication and flexibility in dopant concentration, polycrystalline YAG also benefits from better thermomechanical properties. The first report of Nd:YAG ceramics for laser gain media appeared only in 1995 [12] and three years later the performance was improved to rival its single crystal [18]. There are two methods to make polycrystalline YAG and are discussed in the following sections.

1.2.1 Nonreactive sintering

One of the ways of obtaining YAG ceramics is to sinter green bodies of YAG powder and the method is termed as nonreactive sintering. This method has been particularly developed by Konoshima Corporation in Japan. Limited description of this process exists in the literature. Other approaches included the synthesis of YAG particles by spray-pyrolysis. De With and Van Dijk [19] prepared transparent YAG samples via vacuum sintering at 1850°C for 4 h using YAG powders synthesized by a sulfate co-pyrolysis method. Li *et al* [20] produced YAG powders via co-precipitation method. Yttria and alumina salt precursors are co-precipitated at room temperature. After calcination of the dried co-precipitate, nanoparticles of YAG are formed. This method provides well-sinterable YAG particles and allows more intimate mixing of yttrium and aluminum than the solid-state synthesis method. There exists several methods to shape YAG powders, Konoshima Corp. uses the slip-casting method in which a porous mold is filled with a slurry of YAG powders with containing a dispersant and a binder. The liquid is sucked by the porous mold which forces the powder to take its shape and forms a compact green body. With this method the relative density of the green bodies can reach 64% a value corresponding to the relative density of powder in a random close packing arrangement. ***The problem with this technique is that the coprecipitation of yttrium and aluminum salts may not be homogenous resulting in nonstoichiometric YAG powder. Moreover, the technique is very time consuming and the yield is low.***

1.2.2 Reactive sintering

Another technique to fabricate YAG ceramics, developed by Ikesue [12], is called reactive sintering. In this technique Al_2O_3 and Y_2O_3 powders are mixed in a stoichiometric ratio, compacted

into pellets and subjected to high temperature so that solid-state chemical reaction and densification occurs simultaneously. The starting oxides are put together in a jar with ethanol as a dispersing medium and TEOS (tetraethylorthosilicate) as a source of silica which acts as a sintering aid. This mixture is ball-milled with alumina balls for 5 to 12 hours. This has two effects: the homogenization of the particles size (dispersion of soft agglomerates), and the intimate mixing of the raw oxides. The slurry is then dried and shaped by cold uniaxial pressing. To further increase its density before the sintering, the green body is cold isostatically pressed at 200MPa. Usually after this stage, densities of 45-55% (relative to the single crystal) is achieved. The pellet is then sintered under vacuum (under ~10^{-5} Torr) at a temperature of 1650°C to 1800°C to form YAG ceramics. Despite several issues, described in the following section, the reactive sintering technique is much cheaper, easier and faster than the wet chemistry approach and has, for this reason, been a very popular technique in the fabrication of YAG transparent ceramics since 1995.

1.3 Factors affecting the optical properties of YAG TOCs

The most important scattering sites in polycrystalline YAG are the secondary phases and residual porosity [21], while absorption loss are caused by dopants and contaminants [15]. We will now discuss the extent of their effect and the difficulties in avoiding these defects.

1.3.1 Point defects and secondary phase precipitation caused by non-stoichiometry

One of the most pressing problems with the fabrication of YAG ceramics is guaranteeing the repeatability of the process from one batch to the next. This difficulty can be better understood by looking at the Al_2O_3-Y_2O_3 phase diagram (figure 3). Following the figure form left to right, the first stable phase is the yttrium aluminum monoclinic (YAM, $Y_4Al_2O_9$) at Al/Y molar ratio of 1:2.

Increasing the alumina content further, yttrium aluminum perovskite (YAP, $YAlO_3$) is formed at the molar ratio of 1:1. Further to the left, YAG is formed when molar ratio reaches 5:2. In reactive sintering, YAG phase is formed according to[4] [22]:

(a) $2Y_2O_3 + Al_2O_3 \rightarrow Y_4Al_2O_9$ (YAM), occurs at temperature range 1173-1373K [23]

(b) $Al_2O_3 + Y_4Al_2O_9 \rightarrow 4YAlO_3$ (YAP) , occurs at temperature range 1373-1523K [24]

(c) $Al_2O_3 + 3YAlO_3 \rightarrow Y_3Al_5O_{12}$ (YAG), occurs at temperature greater than 1523K [24]

From step (c) it can be inferred that excess of yttria and alumina can lead to precipitation of YAP and Al_2O_3 respectively. Due to the larger surface energy, they are more likely to nucleate at the grain boundaries [25]. The amount of phase precipitation depend on the extent of non-stoichiometry, the amount of dopant introduced in the material, sintering temperature, the cooling rate after sintering and solid solubility limit of YAG which is not well known [26]. Zhu *et al* [15] could not detect the presence of secondary phases using X-ray diffraction (XRD) when yttria was put in excess of up to 2.9 mol%, whereas similar analyses by Qin *et al* [17] did not see these phases up to 1 mol% extra alumina and 2 mol% extra yttria. In the latter case, the sample appeared translucent at 0.5 mol% excess alumina suggesting the presence of a secondary phase precipitation. Patel *et al* [27], again by XRD analysis, but this time looking at the effect of point defects on the dimension of the unit cell, suggested that the solid solubility limit extends to 0.45 mol% on the alumina side and 1 mole% towards the yttria side (i.e. 62.07 to 62.61 mol% of Al_2O_3, respectively in figure 3), a much narrower solubility range than suggested by previous studies. The rather low sensitivity of phase identification by XRD for small amounts of crystalline precipitates, the solid

[4] Although the details of the solid-state reaction are not as simple as this linear sequence.

solubility limit may be narrower than suggested by ref [27]. The secondary phases are a prominent scattering sites because of the difference in refractive index with YAG phase. Since Al_2O_3 is less soluble in YAG, tiny variation of alumina in the starting powered has severe consequences on the optical quality of the final ceramic. Within the solid solubility limit, the excess of alumina or yttria is accommodated by the formation of antisite defects [27, 28]:

Al_2O_3 excess: $4Al_2O_3 + 3Y_Y^X \leftrightharpoons 3Al_Y^X + Y_3Al_5O_{12}$ (0.2 eV)

Y_2O_3 excess: $Y_2O_3 + Al_{Al}^X \leftrightharpoons Y_{Al,16a}^X + YAlO_3$ (-0.02 eV)

These defects can contribute to absorption loss. However, the position of their energy levels in the bandgap may form efficient trapping sites for charge-carriers and thereby affecting the performance of scintillators and phosphors.

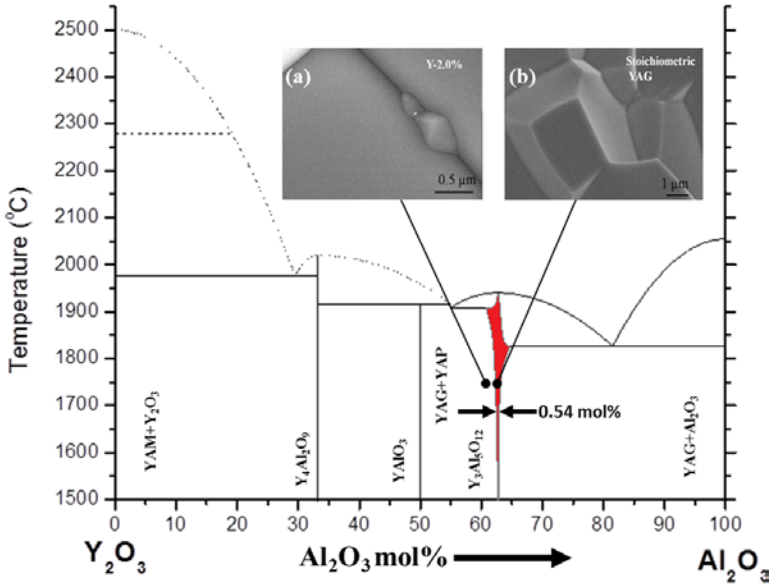


Figure 3. Y_2O_3-Al_2O_3 phase diagram. Inset (a) 2 mol % excess yttria which causes the precipitation of YAP at the grain boundary. (b) Stoichiometric YAG with clean grain boundary

The disparity in the composition can arise during powder weighing and the ball milling process. For better sinterability, powder sizes smaller than a micron are preferred [25]. Such small-sized powders have propensity to adsorb moisture and can offset the weight measurement. Typically, the amount of moisture adsorbed in the alumina and yttria powders used in our lab and calculated using thermogravimetric analyzer (TGA), is 0.6732±0.0331% and 0.7149±0.0201% respectively. The error can also come from the weighing balance itself, which is typically less than 0.2 mg. The excess of alumina coming from ball milling is hard to quantify as it depends upon the amount powder grinded and the speed at which the mill is rotated. In one of our experiment, we noticed that the powder mixture with alumina to yttria molar ratio of 1.6209, which is well outside the estimated solid solubility limit, turned transparent. Recollecting that the ceramics within the range $\frac{4.910}{3} < \frac{\mathrm{Al}}{\mathrm{Y}} < \frac{5.008}{3}$ turn transparent, the shift in the ratio most likely lies within 0.02 to 0.05. From this, the amount of alumina coming from the grinding balls is estimated to be 1.31±0.6 mol %. This clearly shows that the contamination from ball milling is by far the largest contributor to non-stoichiometry. Also, due to the large uncertainty in this estimation, adjusting the alumina content in the initial mixture may not yield the right stoichiometry. At first glance it might look like substituting the alumina balls with other abrasive such as titanium nitride or zirconia may solve the problem but this will bring undesired contaminants and associated defects. ***The best way to resolve this problem is to precisely quantify the alumina-to-yttria molar ratio post ball milling and account for this while mixing the powders.*** The ratio of the major elements also needs to be quantified if controlled amount of non-stoichiometry is needed for defect engineering purposes [15]. For instance, by purposely adding extra yttria to create Y_{Al} antisite defects, YAG can be used as an x-ray scintillator. The x-ray excited luminescence intensity increasing with the number of

these defects and at Al/Y molar ratio of 1.47 the luminescence intensity is very close to that of $PbWO_4$, an excellent material for high-energy radiation detection [29].

1.3.2 Residual pores

Complete elimination of the residual pores is one of the most difficult challenges in transparent ceramics fabrication. The large refractive index difference between these gas filled pores and the bulk of the ceramic makes them much more efficient scattering sites than the secondary phases. The extent to which size and volume fraction of porosity influences the laser slope efficiency of Nd:YAG has been well documented. For example, A. Ikesue *et al* [30] showed that the slope efficiency of 1.1 at%Nd:YAG ceramics reaches that of a single crystal, at laser outputs in the 100s mW range, only when the concentration of the pores is reduced below 150 ppm. More recently, Boulesteix *et al* [31] has shown that for laser operated in mJ range, the pore concentration should be less than 18 ppm for 1at%Nd:YAG. The highest output power achieved in reactively sintered Nd:YAG is 2.4 kW but the authors have not specified the volume fraction of the pores which could be clearly seen in the TEM images [32]. Judging from the porosity of Konoshima samples, in which laser power up to 25 kW has been obtained [33], the pore concentration must be ~1 ppm. It is to be noted that the laser performance does not depend on pore concentration alone but also on the amount of impurities and dopant. Nevertheless, these results show that for high power laser application, pores should be virtually non-existent.

1.3.3 Impurities

Impurities in Nd:YAG samples can be either intentional or unintentional and can negatively impact the laser performance. Intentional impurities, also called dopants, are either

added to provide optical functionalities (lasing ion, fluorescence, energy transfer, etc.) or assist the densification process by removing residual porosity. For example, in reactively sintered Nd:YAG ceramics, densification is usually achieved by adding silicon dioxide (SiO_2) [34-36]. It is blended with the starting powders in the form of fine soot or via liquid precursor (tetraethyl orthosilicate, TEOS). TEOS decomposes into SiO_2 by hydrolysis with water adsorbed on the powder surface and is usually preferred over SiO_2 soot to achieve better homogeneity. Increasing the dopant concentration results in the reduction of both sintering time and temperature and no secondary phase segregation is observed up to 0.28 wt% SiO_2 doping in Nd:YAG [26, 37]. Silica prevents abnormal grain growth and greatly reduces the amount of closed pores which helps achieve more than 99.999 % of theoretical density. It has been shown that the rate limiting factor in the densification of YAG ceramics is the grain boundary and lattice diffusion of rare earth ions [37, 38]. Silicon promotes the densification kinetics by creating yttrium vacancies and thus facilitates the grain boundary and lattice diffusion of Y^{3+} and Nd^{3+}. Since these ions migrate by vacancy hopping, the self-diffusion constant of rare-earth ions in YAG is directly proportional to the yttrium vacancy concentration. Despite the general consensus on the densification mechanism at play in this material, there are two conflicting explanations regarding the evolution of grain growth at the end of the sintering process. R. Boulesteix *et al* [37] found that SiO_2 forms a liquid phase with YAG at the sintering temperature (~1750^{o}C) and grain growth occurs via Ostwald's ripening. A. Stevenson *et al* [26], on the other hand, concluded that grain growth occurs via solute drag. In these studies, the actual amount of silica in the final stages of sintering is not known as it can escape the system during vacuum sintering [21, 39]. ***To fully understand the sintering process, it would be therefore beneficial to know the concentration of remnant silicon in the sintered***

ceramics. If TEOS is used for incorporating silica, there can be larger uncertainty in SiO_2 content either due to incomplete hydrolysis or evaporation during powder drying.

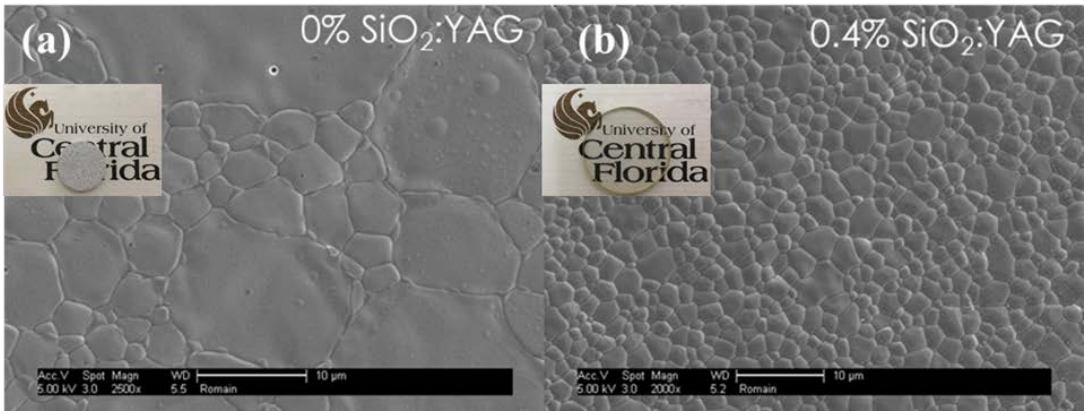


Figure 4. Effect of SiO_2 sintering aid on the densification of YAG ceramics: (a) abnormal grain growth and closed pores due to the lack of sintering aid (b) uniform grain growth with virtually non-existent porosity because of SiO_2 addition yielding a transparent sample.

Though SiO_2 is indispensable for obtaining a high degree of transparency in YAG ceramics and better results are obtained by increasing the doping level , it can have negative impact on the laser performance. It has been shown both by atomistic simulation [28] and experimentation [26] that Si^{4+} ion occupies the tetrahedral Al^{3+} sites. In a reducing atmosphere, as in the case of vacuum sintering, Si^{4+} reduces to Si^{2+} and enters the octahedral Al^{3+} site, leaving a negatively charged oxygen vacancy behind [40]. The proximity of Si^{2+} with the oxygen vacancy forms an impurity-stabilized color center (F_A center) with absorption bands extending from the near infrared (NIR) to the UV, thereby affecting the lasing wavelength of Nd:YAG. The concentration of these color centers depends on the silicon concentration and on the oxygen partial pressure according to the following relation:

$$[F_A] \propto [Si] P_O^{-1/2} \quad (1)$$

Thus, to reduce the absorption loss associated to silicon-induced color centers, either the amount of silica must be reduced or the partial pressure of the oxygen should be increased. This requires an optimization in the initial amount of silica introduced into the ceramics and the annealing protocol after sintering.

The concentration of unintentional impurities, such as Fe, Ca, Mg, Co etc. is typically less than 10 ppm [41] when care is taken to handle powders and green bodies away from stainless steel equipment and plaster of Paris slip-casting molds. The extent to which these ions degrade the laser performance is known and results in absorption bands in the NIR and visible [28] and photodarkening effects [39]. ***Hence, for quality control purposes, it would beneficial to identify, quantify and determine the source of these contaminants throughout the ceramic fabrication process.***

1.4 Previous studies on the quantification of non-stoichiometry and impurities in YAG

The measurement of elemental ratios of Al to Y in YAG by ICP-AES has been mentioned in few articles but the results are not presented [15, 17]. Also, the shift from the garnet stoichiometry in those samples exceed the solid solubility limit. The first publication specifically addressing this issue was reported by Patel *et al* [27] by measuring the change in lattice parameter with stoichiometry shift but the relationship between these parameters was not monotonic and the sensitivity was too low to separate samples close to stoichiometry (figure 5). Another attempt was made to quantify the shift in stoichiometry by measuring the change in terahertz spectrum of YAG

with non-stoichiometry (figure 6). Although the absorbance varies with non-stoichiometry, this technique cannot distinguish excess of yttria from excess of alumina.

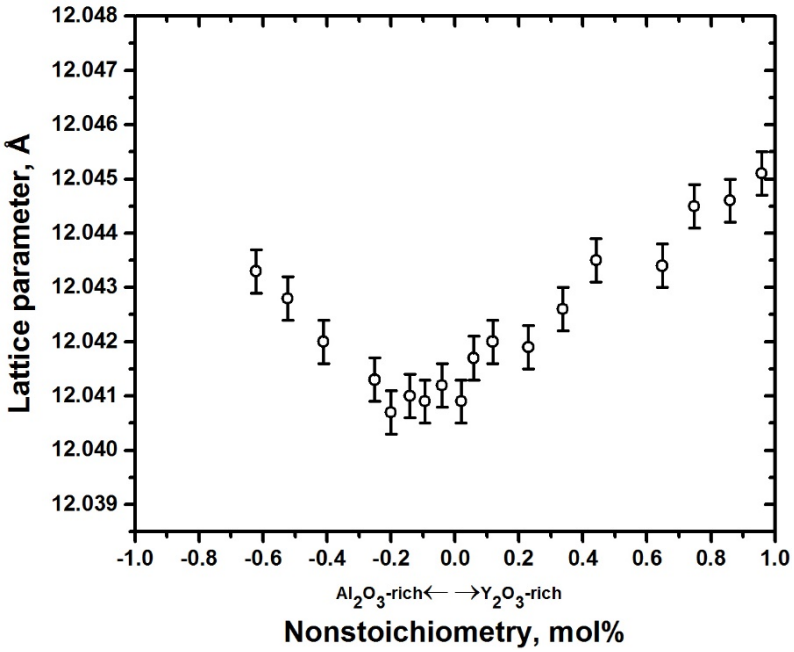


Figure 5. Variation of YAG lattice parameter with non-stoichiometry.

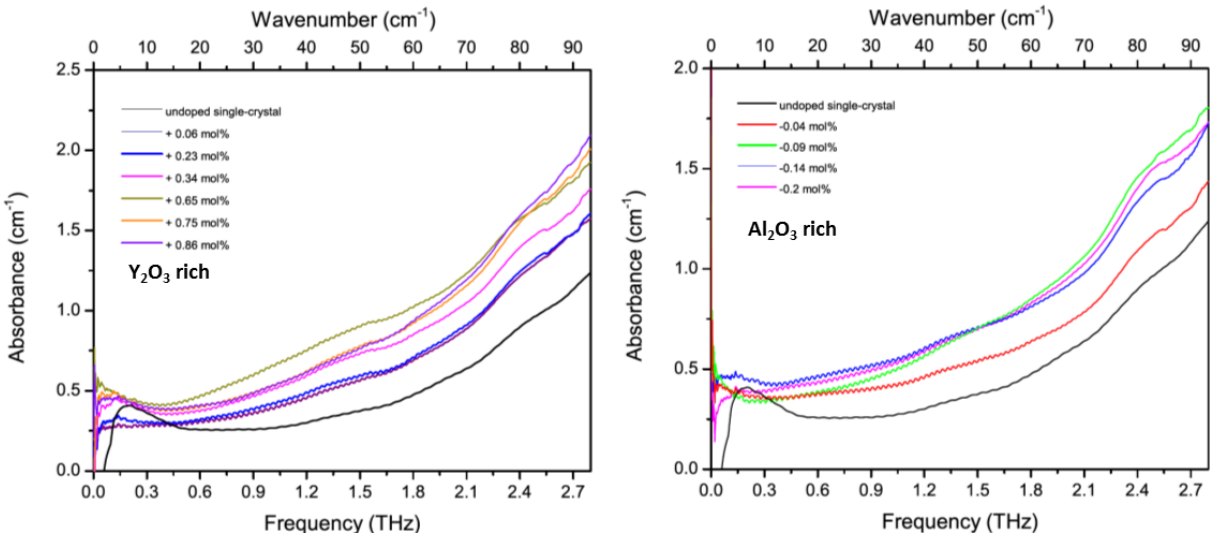


Figure 6. Variation of terahertz spectrum of YAG with non-stoichiometry.

1.5 LIBS as an analytical tool for the quantification of non-stoichiometry and impurities

LIBS is an elemental quantification technique that utilizes plasma created by high power laser for atomic emission spectroscopy. It has been established as a versatile technique for elemental analysis [42-44]. The technique is inexpensive compared to ICP-AES, XRF, ICP-MS and other mass-spectrometry based techniques [45]. It can detect all the elements in the periodic table, has simultaneous multi-elemental analysis capability, requires little or no sample preparation and imparts minimal damage to the samples. LIBS can be used to analyze solid, liquid or gaseous samples for qualitative and quantitative purposes [46]. Furthermore, the instrument is well suited in a laboratory setting because of its small footprint compared to other techniques mentioned above. The aforementioned traits along with its potential for real-time, *in-situ* application [47] have attracted LIBS to many fields such as metallurgy [48, 49], ceramic processing [50, 51], environment [52-55], geology [56-58], biology [59, 60] and forensics [61-64]. However, most of these applications focus on the quantification of trace or minor elements. The quantification of major elements by LIBS is hindered by self-absorption, an aspect we will discuss in detail in Chapter 2. Nevertheless, there are some promising reports of compositional analysis of major elements in thin films [65-68] and we saw that standard analysis LIBS protocols could possibly be adapted to our particular problem.

1.6 Summary and dissertation outline

This thesis is motivated by the lack of fabrication consistency of YAG transparent optical ceramics and proposes an approach to solving the observed batch-to-batch fluctuations in optical quality, by providing a reliable and sensitive analytical method to measure:

(1) stoichiometry shifts, and

(2) the concentration of sintering additive

at the various stages of the fabrication process of multinary TOCs. We propose the use of LIBS with revised modalities and protocols to aid us in this challenging determination. Our study is going to be based on reactively sintered ceramics of Y_2O_3-Al_2O_3 mixtures near the garnet composition and with varied Al/Y molar ratio ranging from 1.6 to 1.67 with a step size of 0.007. The quantification of SiO_2 sintering additive will be carried out on green bodies, calcined samples and fully sintered ceramics.

This manuscript is divided into seven chapters. In Chapter two, fundamentals of atomic emission spectroscopy relevant for the LIBS experiments are presented followed by the basics of the LIBS hardware and the pitfalls that needs to be avoided during the experiment.

Chapter three gives the results of the LIBS plasma simulation which was performed to calculate the number density of different ionic and neutral elemental species. This calculation helps identify the plasma temperature range in which the LIBS signal is most sensitive to variations in the Al/Y molar ratio.

Chapter four details the LIBS experiment on YAG ceramics to discern the Al/Y molar ratio. First, the fabrication process of the YAG ceramics by reactive sintering is detailed after which the assembly of the LIBS system is described. Finally, the result of the experiment and its broader implications are discussed.

Chapter five explores the possibility of using LIBS to quantify stoichiometric inconsistency and impurities at the early stages of the ceramic fabrication. The experiment is

performed on powders and powder compacts to investigate the fluctuation in LIBS signal with sample compaction density.

Chapter six presents the result of LIBS experiment that follows the concentration of silicon in YAG samples in different stages of fabrication.

Finally, Chapter seven summarizes our results and offers suggestions to improve the sensitivity and performance of our setup

CHAPTER TWO: ATOMIC EMISSION SPECTROSCOPY AND LIBS

Laser-induced breakdown spectroscopy belongs to a class of optical emission spectroscopies (OES) in which the wavelength of the light emitted by atoms, ions, or molecules is monitored during their transition from an excited to a lower energy state. Because each of these species has a unique emission spectrum according to its electronic, vibrational and rotational structure, the examination of the emitted light can provide valuable information about their nature and their concentration. The OES modalities used for the production of emitters in their excited states vary, but before we address the specificities of LIBS, we would like to review some useful considerations regarding the retrieval of concentrations by atomic emission spectroscopy.

2.1 Fundamentals of atomic emission spectroscopy

A spectral line is emitted when a bound electron undergoes a transition from an upper level j of energy E_j to a lower level i of energy E_i. The frequency of the line is given by [69]:

$$\nu_{ji} = \frac{E_j - E_i}{h} \tag{2}$$

The transition is spontaneous and the decay is proportional to the density N_j^z of a species with charge z in the upper energy state E_j. The rate of decay is given by:

$$\left| -\frac{dN_j^z}{dt} \right|_{j \to i} = A_{ji} N_j^z \tag{3}$$

The constant A_{ji} is known as atomic transition probability (unit s^{-1}), also known as the Einstein coefficient of spontaneous emission. A photon is emitted for each transition, and the intensity of radiation is given by:

$$I_{ji} = \frac{h}{4\pi} \nu_{ji} A_{ji} N_j^z \quad (4)$$

This equation reveals that the population densities N_j^z of the excited states can be obtained from measurements of line intensities provided that the transition probabilities are known. Emission is also induced by electromagnetic wave fields and the respective rate is proportional to the spectral radiant energy density u_{ν}:

$$-\frac{dN_j^z}{dt}\Big|_{j\to i} = u_\nu B_{ji} N_j^z \quad (5)$$

The inverse process is absorption,

$$-\frac{dN_i^z}{dt}\Big|_{i\to j} = u_\nu B_{ij} N_i^z \quad (6)$$

B_{ji} *and* B_{ij} are known as Einstein coefficients of stimulated emission and absorption, respectively.

If the ensemble of atoms is in thermodynamic equilibrium (TE), the population of upper level *j* relative to that of the ground state is given by the Boltzmann distribution:

$$\frac{N_j^z}{N_0^z} = \frac{g_j}{U^z(T)} e^{-\frac{E_j}{kT}} \quad (7)$$

Here, g_j is the degeneracy of the exited state *j*, U^z the partition function for a charge state *z*, N_0^z the total population of species with charge state *z*, *T* the temperature of the ensemble and *k* the Boltzmann constant. The spectral radiant intensity is therefore given by:

$$I_{ji} = \frac{h}{4\pi} \nu_{ji} A_{ji} N_0^z \frac{g_j}{U^z(T)} e^{-\frac{E_j}{kT}} \quad (8)$$

Rearrangement of equation (8) yields:

$$\ln \frac{I_{ji}\lambda_{ji}}{g_j A_{ji}} = -\frac{E_j}{kT} - \ln \frac{4\pi U^z}{hcN_0^z} \quad (9)$$

Plotting the terms in left-hand side against the upper energy level of the transition yields a straight line with slope $-\frac{1}{kT}$. This so-called "*Boltzmann plot*" technique is frequently used to deduce the temperature of the ensemble [70, 71].

The ground state population of ionic state *z+1* with respect to the ionic state *z* is given by Saha equation [72]:

$$\frac{N_e N_a^{z+1}}{N_a^z} = \frac{2U_a^{z+1}(T)}{\Lambda_e^3 U_a^z(T)} e^{-\frac{E_a^{ion}}{kT}} \quad (10)$$

Here, E_a^{ion} is the ionization energy of species *a* in charge state *z* and Λ_e is the thermal De Broglie wavelength given by $\Lambda_e = \frac{h}{\sqrt{2\pi m_e k_B T}}$, where m_e is the mass of the electron. This equation is constrained by the conservation of species and by the electroneutrality according to:

$$N_a = \sum_{z=0}^{n_{Za}-1} N_a^z,\ z = 0,1,2 \ldots n_{Za} - 1 \text{ and } N_e = \sum_{a=0}^{n_a-1} \sum_{Z=0}^{n_{Za}-1} z N_a^z$$

Here, N_e is the charge density and N_a the number density of species *a*.

Radiation is also emitted when electrons transit between free energy states (free-free transitions). This type of radiation is called *Bremsstrahlung*. Conversely, the release of excess electron kinetic energy upon capture by an ion (free-bound transition) is called *recombination radiation*. These two sources of radiation form a continuous emission background spectrum superimposing the discrete atomic emission lines.

2.1.1 Line broadening

Despite what equation (8) suggests, the radiation emitted by electronic transitions is not infinitely narrow in wavelength, and various factors contribute to spectral broadening [73, 74]. We now review these factors briefly.

2.1.1.1 Natural line broadening

The Heisenberg energy-time uncertainty principle produces the so-called natural line broadening. If the mean time the atom spends in an excited state E_j is Δt_j, then there will be an uncertainty ΔE_j in the value of E_j. This spread in energy level affects the wavelength of the resonance line according to $\Delta\lambda_N = \frac{A_{ji}\lambda^2}{2\pi c}$. Typical values for this broadening amount to 10^{-6} nm in the visible domain, an effect hardly measurable with standard OES instruments and negligible compared to the sources of broadening that follow (~10^{-3} nm) [73].

2.1.1.2 Doppler broadening

In a gas or a plasma, the emitters (atoms and ions) are animated by a Maxwell-Boltzmann distribution of velocities resulting in the Gaussian broadening of the emission lines by an amount [75]:

$$\Delta\lambda_D = \left(\frac{2kT\ln 2}{m_a c^2}\right)^{1/2} \lambda_{ji0} \qquad (11)$$

Here, m is the mass of the emitter, and λ_{ji0} is the central wavelength of transition from j to i.

2.1.1.3 Stark broadening

Likewise, collisions between the emitting species and charged particles in a plasma produce a variable-range Stark field on the emitters that results in a Lorentzian broadening of the emission lines. For neutral atoms, the linewidth due to collisional broadening is approximated by [76]:

$$\Delta\lambda_{Stark} = \left[1 + 1.75A\left(\frac{3}{4}\right)N_D{}^{-\frac{1}{3}}\right] W_{FWHM}\left(\frac{n_e}{10^{16}\mathrm{cm}^{-3}}\right) \quad (12)$$

Here, $\Delta\lambda_{Stark}$ is the full width at half maximum (FWHM) of the line, A a dimensionless coefficient that gives the ionic contribution, n_e the electronic density of the plasma, N_D the number of particles in the Debye sphere, and W_{FWHM} the Stark broadening parameter for the FWHM, a parameter that has been tabulated for many lines of most elements. Electric field that causes Stark effect in laser-induced plasma predominately arises from collision with electrons as they are more mobile than the ions. Neglecting the ionic part of equation (12), one can write:

$$\Delta\lambda_{Stark} = W_{FWHM}\left(\frac{n_e}{10^{16}\mathrm{cm}^{-3}}\right) \quad (13)$$

Hence, equation (13) can be used to determine the electronic density of the plasma, once any instrumental and Doppler broadenings have been taken into account.

2.1.1.4 Convolution of line broadening

In general, the Doppler and Stark broadenings are superimposed. The resulting line shape is a Voigt profile given as follows [77]:

$$\Gamma_v(\lambda) = \frac{2\sqrt{\frac{\ln 2}{\pi}}}{\Delta\lambda_D} K(u,a) \quad (14)$$

where $K(u,a) = \frac{a}{\pi}\int_{-\infty}^{+\infty} \frac{e^{-t^2}}{(u-t)^2+a^2}\,dt$

$$u = \frac{2\sqrt{\frac{ln\,2}{\pi}}}{\Delta\lambda_D}(\lambda - \lambda_{ji}) \tag{15}$$

$$a = \sqrt{ln\,2}\,\frac{\Delta\lambda_N+\Delta\lambda_L}{\Delta\lambda_D} \approx \sqrt{ln\,2}\,\frac{\Delta\lambda_L}{\Delta\lambda_D} \tag{16}$$

Here $\Delta\lambda_N$, $\Delta\lambda_L$ and $\Delta\lambda_D$ are natural, Lorentz and Doppler line width respectively. In addition to the Doppler and Stark effects, instrumental effects (diffraction by the slits and grating of the spectrometer) also contribute to spectral broadening, with both Lorentzian and Gaussian components. Hence, the following formulas should be used to deconvolute the contribution from instrumental broadening:

$$(\Delta\lambda_G^E)^2 = (\Delta\lambda_D)^2 + (\Delta\lambda_G^I)^2 \tag{17}$$

$$\Delta\lambda_L^E = \Delta\lambda_L + \Delta\lambda_L^I \tag{18}$$

Here $\Delta\lambda_G^E$ and $\Delta\lambda_L^E$ are the Gaussian and Lorentzian FWHM obtained experimentally from the Voigt fit to the line profile. $\Delta\lambda_G^I$ and $\Delta\lambda_L^I$ are the Gaussian and Lorentzian components of the instrumental broadening. $\Delta\lambda_D$ and $\Delta\lambda_L$ are the true Doppler and Lorentz line width. With the inclusion of the line broadening, equation (8) modifies to:

$$I_{ji}(\nu) = \Gamma(\nu)\,\frac{h}{4\pi}\nu_{ji}A_{ji}N_0^Z\,\frac{g_j}{U^Z(T)}\,e^{-\frac{E_j}{k_BT}} \tag{19}$$

Here $\Gamma(\nu)$ is the line profile as a function of frequency and depends upon the broadening mechanism. This function is normalized to unity:

$$\int_{-\infty}^{+\infty}\Gamma(\nu)d\nu = 1 \tag{20}$$

2.1.2 Self-absorption

The intensity of the line I_{ji} given by equation (27) may be affected by the optical density of the medium in which the emitter lies. In particular, when the radiation emitted by the source is re-absorbed by atoms of the same species in the lower energy state, the radiation is trapped and does not leave the medium. This self-absorption mechanism can be described simply as follow: the intensity distribution of an emission line is $I_o\Gamma_E(\nu)$, where $I_o$the intensity at the line maximum and $\Gamma_E(\nu)$ is the profile function of emitted radiation. After passing through a layer of absorbing species with a number density n_A, the intensity distribution becomes [78]:

$$I(\nu) = I_0\Gamma_E(\nu)e^{\left[\frac{-\rho\Gamma_A(\nu)}{\Gamma_A(\nu_0)}\right]} \tag{21}$$

Here ν_0 is the central frequency of the line profile, $\Gamma_A(\nu)$ is the absorption line profile and ρ is the absorption parameter given by:

$$\rho \sim B_{ij}\Gamma_A(\nu)n_A \tag{22}$$

Equation (22) shows that ρ increases when the Einstein coefficient for absorption is large, and consequently, ρ is larger for transitions from the ground state. ***Hence, for quantitative analysis, only spectral lines that do not include ground state transitions should be considered. This is an important part of the protocol we will describe later in chapter four.*** The absorption parameter also becomes larger when the number density of species n_A increases in the source. Self-absorption is strongest in the center of the line where absorption reaches its maximum. The extreme case of self-absorption is called *self-reversal,* in which absorption is so large that it leads to a minimum in the intensity profile and ρ > l. Self-reversal is only observed when the radiation source has a strong temperature gradient, and the number densities of the ana1yte are high in both the hotter and the cooler zones.

2.2 Laser-induced breakdown spectroscopy

In LIBS, a pulsed laser beam is focused onto a sample surface and ablates a small portion of the material. A plasma is generated within the material vapor and the surrounding atmosphere. As the plasma starts to decay, the atoms of the constituent elements begin to radiate photons. The emission is spectrally resolved by a spectrometer and recorded. Despite the transient nature of the plasma ball, the type of elemental species and their concentrations present in the material, as well as the plasma temperature and electron density can be deduced from careful spectrum analysis. These are the specificities we would like to address now.

2.2.1 Laser ablation and plasma formation

Attempting quantitative compositional LIBS analysis on ceramic powder compacts or sintered bodies is challenging on several accounts. One of these challenges concerns the expected changes in sample ablation due to variations in laser-to-sample coupling efficiency. The mechanism by which laser energy couples to a material depends upon the characteristics of the laser light (wavelength, pulse duration, energy) and of the material's electronic band structure (namely, if the material is a metal, semiconductor or an insulator). In the case of metals, light is strongly absorbed if its frequency is less than the plasma frequency:

$$\omega_p = \sqrt{\frac{n_e e^2}{m_e \epsilon_0}} \tag{23}$$

with n_e the free electron density in the metal and ε_0 is the vacuum permittivity.

In the presence of a very strong time-varying electric field, such as in pulsed laser light, the electrons get accelerated to very high velocities (inverse bremsstrahlung process) and collisions

with the lattice generate tremendous amount of heat, enough to melt and vaporize the material. When $\omega > \omega_p$, the response of the plasma to the electric field is not fast enough and the absorption coefficient drops off sharply. In the case of semiconductors and insulators, the bound electrons get to the conduction band by means of either linear and/or nonlinear optical processes. These electrons achieve high enough kinetic energies to produce more electrons by impact-ionization. The resulting solid-state plasma is highly absorbing and acts as a mediator to transfer energy from the incoming light into the material lattice in the form of heat. Material ablation occurs if the lattice temperature is raised above the melting point. The typical time scale for free electron heating and thermalization is about 10^{-13} seconds, whereas the collision energy transfer from electrons to the lattice is on the order of 10^{-12} seconds. The time scale for thermal diffusion into the bulk is 10^{-11}s and melting and vaporization take place after a fraction of a nanosecond.

For a given irradiance, the rate of increase of temperature depends upon the thermal and optical properties of the material and also on the properties of the laser beam. The two extreme cases are discussed below [79, 80]:

a) Surface absorption

This case applies when the optical penetration depth, δ_p, is much smaller than thermal penetration depth, δ_h. This situation is encountered in metals and in insulating materials when the energy of the laser radiation is larger than the bandgap. If the beam has a Gaussian profile, the amount of radiation absorbed by the surface is:

$$I_S = AI_0 e^{-\frac{2r^2}{w_b^2}} \tag{24}$$

Here A, I_0, r, w_b are the absorbance, incident intensity, radial distance from the center of the beam and beam waist, respectively. Assuming that all the absorbed energy is converted into heat and that the material property constants are independent of temperature, the heat flow equation can be written as:

$$c_p \frac{\partial T}{\partial t} = \frac{D}{\rho} \nabla^2 T + A I_0 e^{-\frac{2r^2}{w_b^2}} \tag{25}$$

Here c_p, D, T and t are specific heat, thermal diffusivity, temperature and time respectively.

Solution of this equation yields:

$$T = \frac{A I_0 w_b}{\sqrt{2\pi}\kappa} \tan^{-1} \frac{\sqrt{8\kappa t}}{w_b} \tag{26}$$

Here, T is the temperature at the center of the beam and on the sample surface. $\kappa = \rho D c_p$ is the thermal conductivity. Using this equation in metals such as steel and aluminum, it is found that the irradiance of ns-lasers should be greater than 10^8 W/cm^2 for material evaporation. This equation highlights the importance of thermal properties of the material and the beam shape in the ablation process.

b) Bulk absorption

When the optical penetration depth is larger than thermal penetration depth, as glasses, heat conduction can be neglected and only the material directly on the path of laser beam is ablated. The intensity of the beam decreases as it propagates inside the material according to Beer-Lambert law:

$$I = (1 - R) I_0 e^{-\frac{z}{\delta p}} \tag{27}$$

Here *R*, I_0 and *z* are the reflectivity, irradiance at sample surface (z=0) and propagation direction, respectively. The decrease in intensity after traveling a distance *dz* in the material is:

$$dI = \frac{(1-R)I_0 e^{-\frac{z}{\delta_p}}}{\delta_p} dz \tag{28}$$

The amount of laser energy absorbed (*dE*) by volume element *dV* of the material in time interval Δt is then:

$$\frac{dE}{dV} = \frac{(1-R)I_0 e^{-\frac{z}{\delta_p}}}{\delta_p} dt \tag{29}$$

If all this energy is used in heating up the material (i.e. heat capacity), equation (29) can be written as:

$$\rho c_p \Delta T = \frac{(1-R)I_0 e^{-\frac{z}{\delta_p}}}{\delta_p} dt \tag{30}$$

Here, $\Delta T = T - T_0$ is the change in temperature after time *dt* of laser irradiation and T_0 is the temperature of the sample before irradiation. At the sample surface, the temperature evolves linearly with time according to:

$$T = \frac{(1-R)I_0}{\rho c_p \delta_p} t + T_0 \tag{31}$$

Assuming that all the absorbed laser energy is used in evaporating the material and neglecting other forms of energy dissipation (such as shock waves, absorption by the plasma formed on the surface, enthalpy of melting and also the re-deposition of the vapors), the maximum mass of matter ablated can be obtained from energy balance:

$$M = \frac{E(1-R)}{C_p(T_b - T_0)+L_v} \quad (32)$$

Here, E is the energy of the laser pulse, T_b is the boiling temperature and L_v is the latent heat of vaporization. Using this equation for YAG (L_v=6.56×10^3 J/g, c_p=0.59J/gK, T_b-T_0=4000 K) and $E(1-R)$=10mJ we find M=1.12 μg. In the case of pico and nano-second laser pulses, the trailing edge of the laser pulse heats the material vapor and ionizes some of the atoms. The few electrons get accelerated to very high energies and avalanche ionization takes place by inverse Bremsstrahlung process. If the plasma is weakly ionized, a portion of the laser energy penetrates through the plasma onto the material surface and some of it is absorbed by the plasma itself. When the laser energy is high enough, the electron density reaches a critical value and the plasma becomes highly reflective to the beam. This occurs when plasma frequency becomes larger than the frequency of laser light, i.e.

$$\omega_L = \sqrt{\frac{n_c e^2}{m_e \epsilon_0}} \quad (33)$$

Which yields $n_c \sim \frac{10^{21}}{\lambda_L^2}$ cm^{-3}. Here n_c is the electron density, ω_L is the frequency of the laser. This implies that amount of mass ablated will level off after a certain laser energy.

The ablated material gets distributed into the plasma as well as in the form of neutral atoms, molecules or particles. In materials made up of multiple elements (multinary compounds such as YAG), or when several chemical phases are present (such as in ceramic alloys), the volatility of the various elements and the difference in latent heat of vaporization and melting between the phases may cause selective vaporization. To overcome this problem, either the laser energy must be higher than the latent heat of vaporization of all the constituents or the vapors must be formed

by desorbing atoms by photochemical process. This can be achieved by laser with pulse duration shorter than the time scale for thermal diffusion (sub-picosecond laser pulses). It has been shown that for long laser pulses in the microsecond regime and low irradiances ($<10^6 W/cm^2$), the thermal nature of the process leads to differential vaporization. Conversely, in the nanosecond pulse regime, and at irradiances greater than 10^9 W/cm^2, the pressure over the surface inhibits further vaporization until the substrate reaches a critical temperature. ***Under these conditions, the uniform heating and the explosive release of the ablation process, favor a so-called 'stoichiometric ablation', in which the compositions of the ejected melt is the same as that of the sample. These conditions are crucial to our approach.***

2.2.2 Characteristics of a LIBS plasma

Our approach also relies on a critical synchronization between the ignition of the plasma and the detection of the spectral lines emitted by the species of interest. An example of temporal evolution of LIBS plasma obtained on aluminum oxide powder is shown in figure 7. The gate delay in the z-axis is the time interval between the moment the laser strikes the sample surface and the acquisition of spectrum.

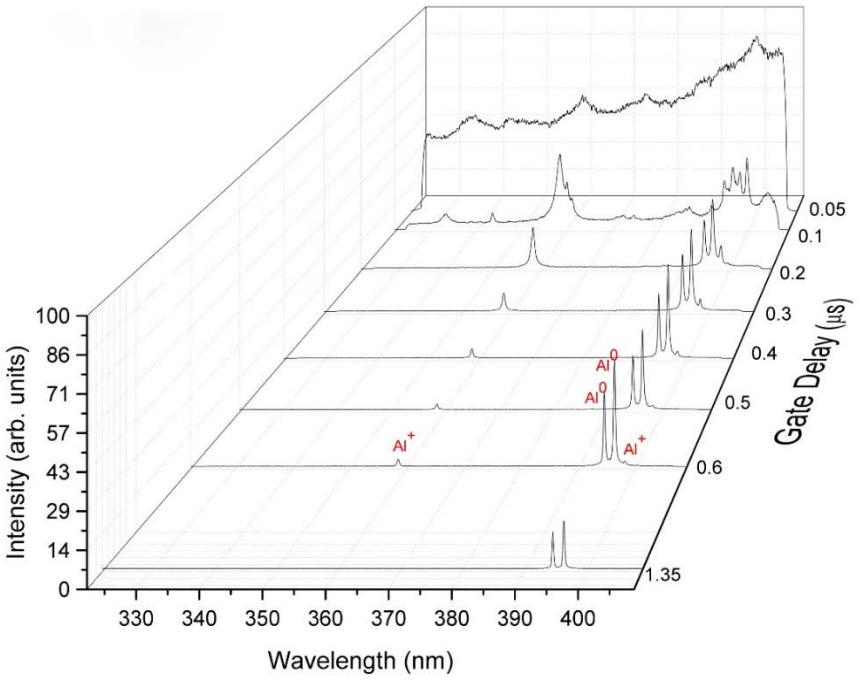


Figure 7. Temporal evolution of LIBS plasma in aluminum oxide pellet. The laser energy and gate width was set at 8 mJ and 50 ns respectively

This particular experiment was done in aluminum oxide powder and shows that before 100 ns, the spectrum is dominated by the continuous background. At these times, the plasma is very hot and highly ionized. The radiation is due to Bremsstrahlung and recombination. At times larger than 100 ns, radiation due to transition of electrons from atomic levels begin to appear. As the plasma evolves and cools down, the emission from ionized species begins to fade, while that from neutral species begins to dominate until about 600 ns. ***This example highlights the fact that optimized time-gated detection allows for selective information to be recovered.***

Now that we have reviewed the main trade-offs in laser-induced breakdown spectroscopy, we will now examine the experimental setup implemented to perform our studies.

2.3 Components of LIBS system

The basic components required for LIBS are the excitation source, some collection optics to focus the radiation from excited atoms into a spectrometer, a diffraction grating to resolve the light into individual wavelengths and a device to record the spectrum.

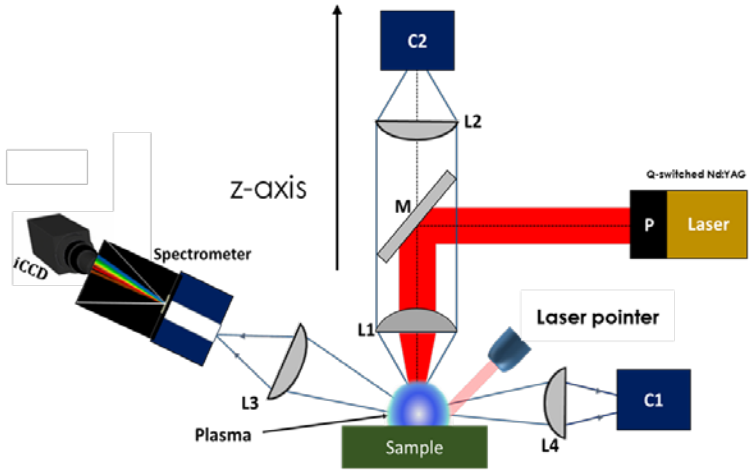


Figure 8. Schematics of a typical LIBS setup. The laser shown here is a 1064 nm Q-switched Nd:YAG. M is a dichroic mirror that is highly reflective above 1000 nm. L1 is the lens to focus laser on the sample surface. L2 and L4 are lenses to focus plasma light into CCD camera C2 and C1 respectively. Lens L3 focuses plasma light into the spectrometer

2.3.1 Laser

In LIBS, contrary to most AES techniques, both the atomization of the sample material and the excitation are brought about by focused high power laser [81]. As shown in earlier section, the power required to achieve vaporization in a material lies in the gigawatt range. Such high power can be achieved by Q-switched lasers, such as Nd: YAG. Its fundamental frequency of 1064 nm can be shifted to wavelengths in the visible or the UV by the use of second harmonic generation.

As discussed before, the choice of wavelength is determined by how well it couples with the sample. Typical pulse duration of this type of lasers is 5 to 8 ns. The pulse energy must also be optimized so that the ablation is sufficient enough to yield stoichiometric ablation and spectra with high signal-to-noise ratio. Using much higher energies than the ablation threshold is not useful, as the amount of ablated material eventually reaches a plateau with increasing pulse energies. The pulse-to-pulse fluctuations in laser energy affect the ablation rate, the temperature of the plasma, and the intensity of the emission lines. Finally, one must pay attention to the spatial quality of the beam as, in order to achieve the irradiance needed to ablate the material, the laser beam must be focused to a sufficiently small size, typically below 100 μm. Hence, TEM 00 or top-hat beam profiles are preferred.

2.3.2 Focusing Optics and plasma light collection

The focusing optics usually consists of a beam expander to reduce the fluence on the optical components and mode-cleaning apertures, and of a terminal lens or mirror to focus the laser beam onto the sample. The damage threshold of these parts and optical coatings must be high enough to withstand the highest peak intensity used in the experiment. The focal length of the lens must be judiciously chosen. Generally, the light coming out the laser has a Gaussian profile. The waist of the beam (w_{02}) after being focused by lens with focal length f is given by [82]:

$$w_{02} = \frac{\lambda f}{\pi w_{01}} \tag{34}$$

Here, w_{01} is the waist of the beam before being focused. The corresponding Rayleigh range is:

$$Z_{02} = \frac{\pi (w_{02})^2}{\lambda} \tag{35}$$

Equations (42) and (35) suggest that using lens of small focal length will make the Rayleigh length of the focused beam small. As a consequence, a small change in the distance between the focusing lens and the sample surface will cause the irradiance to vary significantly. For example, the Rayleigh length of a beam, with initial waist of 5 mm, focused by 1.5 cm focal length lens is 10 μm. This implies that a 10 μm change in the lens-to-sample distance near the focal distance will change the irradiance by as much as 100%. On the other hand, if a longer focal length is used, the spot size will be large and the irradiance may not be sufficient for to ablate the sample.

The collection optics must have a high transmission from the UV to the near IR as most of the atomic emission lines lie in this range. In the case of YAG, the line of interest are in the range 200 nm to 400 nm for both aluminum and yttrium [83]. The lenses made from fused quartz or CaF_2 have this property.

2.3.3 Spectrometer

In order to get the information about the atomic constituents, this light coming out of the plasma must be spectrally resolved. For this purpose, the light is fed into a spectrometer via an optical fiber. The grating of the spectrometer determines its dispersive power as a measure of how well the instrument can resolve closely separated emission lines. It is defined as the change in angle of diffraction per unit change in wavelength. If the grating consists of *N* transparent grooves per unit length, the dispersive power of the grating for n^{th} order maximum is given by:

$$\frac{d\theta}{d\lambda} = \frac{nN}{\cos\theta} \tag{36}$$

where θ is the angle between normal to the grating and the diffracted beam. This formula can be cast into a more experimentally useful form showing the linear spatial separation, *dx*, between two emission lines of wavelengths λ and λ+dλ on the detector:

$$\frac{dx}{d\lambda} = \frac{fnN}{\cos\theta} \tag{37}$$

Hence, the groove density must be high in order to resolve closely spaced lines. For instance, if Al 281.61 nm and Y 278.53 nm peaks are chosen to investigate the composition of YAG samples, NIST atomic spectra database show that a resolution of at least 0.2 nm is required to prevent inter-element spectral interference. This means that the spectrometer for this experiment should have a resolution of at least 0.1 nm. Commercially available spectrometer such as Princeton Instrument SpectraPro 2500i with groove density of 12000 1/mm will meet this criteria.

2.3.4 Device for recording the spectra

The diffracted light from the grating must be recorded on a charge-coupled device (CCD) imaging sensor. It consists of two dimensional array of photoactive pixels which convert light into an electric charge. The size of a pixel ranges from 13×13 μm to 26×26 μm. The charge is then transferred down each column and the last pixel dumps the charge into amplifier which converts it into electrical voltage for recording purpose. Due to fleeting nature of LIBS plasma, as explained in section 2.2.2, the accumulation of spectral data should be properly timed with respect to the firing of the laser. To meet this requirement, an external delay generator should be used for timing purpose if CCD is used for recording the spectrum.

The most popular recording device for LIBS experiments is the intensified charged-coupled device (ICCD) which can be internally gated without the need for extra delay generator.

Modern ICCD camera such as Andor iStar have pico-second resolution in gate width and delay and are well suited for LIBS experiments.

2.3.4.1 Wavelength calibration

After the light gets through the grating and falls on the detector, individual emission lines are registered in different pixels. The software that controls the CCD or the ICCD assigns each pixel to a wavelength. To precisely allocate the peak positions in a given window of the spectrum to a specific element, the assignment of pixel positions needs to be calibrated. It can be done by using an emission spectrum of an element whose peak positions are well known. The element specific lines are compiled in a NIST database [83]. Once the peak positions in the spectrum are identified, they are plotted against their pixel position. Usually, a quadratic fit the data points best. ***This wavelength calibration is a very important aspect of a LIBS analysis which allows the spectral peaks to be properly assigned to their respective emitters.***

2.3.4.2 Spectral response calibration

The response of the detection system and different optical components that direct the light into it are, in general, wavelength dependent. This means that for the same intensity, but different wavelength, the pixels on which they fall may give different readings. In addition to that, the detector response is in photon counts and needs to be changed into the units of spectral radiance. To this end, a calibrated lamp with known spectral intensity distribution must be used. The geometry between the collection optics and the light source should be same as that between the collection optics and the LIBS plasma.

Let I_λ^{Lmap} and $I_\lambda^{Spectrometer}$ be the true spectral intensity of the lamp provided by the vendor ($\mu Wcm^{-2}nm^{-1}$) and the spectral intensity registered by the detector respectively at a particular spectral window. The spectrometer response of any arbitrary spectrum (S_λ) can now be corrected by multiplying it with the transfer function given by $T_\lambda = \frac{I_\lambda^{Lmap}}{I_\lambda^{Spectrometer}}$, i.e. the correct spectrum is given by:

$$S_\lambda^{Corrected} = S_\lambda \times T_\lambda \tag{38}$$

It is to be noted that the spectral response obtained in this manner is not absolute. For all analytical purposes, only relative spectral response is needed.

2.4 Quantitative elemental analysis by LIBS

Generally, quantitative elemental analysis by LIBS is calibration-based. For measuring trace and minor amount of impurity in a sample (for instance SiO_2 in YAG), standard samples with fixed matrix are spiked with different concentrations of the analyte. LIBS experiments are performed with the same experimental conditions on all the samples and the detector response is plotted against the concentration of the analyte. If the composition of matrix itself need to be determined, for instance Al/Y molar ratio in YAG, samples with slightly varying Al/Y molar ratio is prepared and Al/Y intensity ratio is plotted against the molar ratio. If the calibration curve is linear, the slope of the curve is called the sensitivity. If, however, the curve is not linear yet can be represented by a monotonically increasing function, the sensitivity is defined as the slope of the tangent at the middle of the working range. The unknown molar ratio or the concentration of the

analyte is determined by putting the value of the detector response in the calibration curve equation. In the case of trace analysis, the detection limit of the instrument is defined as:

$$LOD = \frac{3\sigma}{m} \quad (39)$$

The limit of quantification, i.e. the minimum concentration of the analyte which can be quantified, is defined:

$$LOQ = \frac{10\sigma}{m} \quad (40)$$

Here, σ is the standard of detector response for blank sample and *m* is the sensitivity.

2.5 Factors affecting the quantitative elemental analysis by LIBS

Elemental quantification by LIBS is simple in principal but some precaution need to be taken while doing the experiment and configuring the apparatus. There are a number of variables that can cause the intensity of the signal to fluctuate for the same amount of analyte in the matrix. Most of these variables have been covered in the earlier sections and are contextualize in this section for quantification purpose. The most important variables that need to be controlled are explained in the following sub-sections. These considerations have been used as general guidelines for designing experimental protocols for the analysis of non-stoichiometry and impurities in YAG.

2.5.1 Laser irradiance on the sample surface

As explained in section 2.2.1, amount of mass ablated from the sample surface depends on intensity of laser falling on it. This means that for the same analyte concentration, the intensity of

spectral lines will vary if the laser intensity fluctuates. The intensity of the laser beam falling on the sample surface is given by:

$$I_{Laser} = \frac{E_{Laser}}{At} \tag{41}$$

Here, E_{Laser} is the laser energy, A is the laser spot size on the sample surface and t is the laser pulse duration. The standard deviation in laser energy and pulse width is fixed for a given laser during the time period of experiment but the spot size will change, as shown in section 2.3.2, if the distance between the laser focusing lens-to-sample surface changes provided that the focal length of the lens is fixed. The two common techniques by which the focusing lens to sample surface distance is kept constant during the experiment are autofocusing [84] and the parallax based methods [85]. In the imaging based technique, a CCD camera (C1 in figure 8) is used to capture the image of the sample surface and the variance of pixel intensity value is calculated at each z position according to the formula:

$$\sigma(z) = \frac{1}{HW}\sum_x \sum_y \left(i(x,y) - \bar{i}\right)^2 \tag{42}$$

Here, σ(z) is the variance of intensity of pixel at positon (x,y), $\bar{i}$ is the average intensity, H and W the dimension of the matrix related to the captured image. At a particular z, σ is maximum and the image is the sharpest. It was shown in ref [86] that the z position at which the variance is maximized is spread over few tens of micron and as demonstrated in section 2.3.2, will cause significant change in intensity from shot-to-shot. To overcome this difficulty, parallex based technique is used where a laser pointer is directed towards the sample in an oblique fashion and the light reflected off the sample surface is focused by lens onto the CCD camera C1. The barycenter of the image is calculated according to the formula:

$$\overline{x} = \frac{\sum_{x,y} x \cdot i(x,y)}{\sum_{x,y} i(x,y)} \quad (43)$$

$$\overline{y} = \frac{\sum_{x,y} y \cdot i(x,y)}{\sum_{x,y} i(x,y)} \quad (44)$$

In the field of view of the camera, the barycenter of the laser spot is very sensitive to the vertical positioning of the sample surface and allows for locking the lens-to-sample distance with an accuracy better than 5 μm [86, 87].

2.5.2 ICCD timings

The LIBS plasma is dynamic in nature, as shown in section 2.2.2. The relative number density of charged and neutral species of an element are changing with time. The time delay and the duration for recording the spectrum must be optimized for the best signal-to-noise ratio and should be kept constant throughout the experiment.

2.5.3 Choice of emission lines

The emission lines for building a calibration curve should be judiciously chosen. As emphasized before, the line emitted due to transition involving the ground state should not be chosen as these lines are prone to self-absorption, i.e. the plasma should be optically thin for that wavelength. The line should also be free of spectral interference and if possible, should be well separated from other emission lines.

2.5.4 Ambient conditions

The effect of background gas and pressure on the LIBS spectrum and hence the analytic figure-of-merit has been well documented in the literature [88-90]. Reduction of background

pressure to few Torrs greatly improves the signal-to-noise ratio and enhances the intensity of the emission lines. Also, a better signal is obtained in argon atmosphere compared to atmospheric conditions.

2.5.5 Matrix effects

Chemical composition [91], density, particle size, moisture content [92] and optical properties of the sample [93] can greatly influence the LIBS signal. This so-called “matrix effect” is due to differences in laser-sample coupling, plasma temperature and electron number density. This is one serious issue in calibration-based quantitative elemental analysis by LIBS, which can be avoided if the calibration sample and the sample with unknown composition have the same characteristics.

2.6 Internal standardization

The surface of the matrix may not be homogenous in density, optical properties and analyte concentration. The intensity of the laser may also vary from pulse-to-pulse. This means that the plasma generated by each laser shot on different spots of the sample surface may not have the same electron number density, temperature or composition. As a consequence, the intensity of the analyte peak varies and the standard deviation may be significant. To minimize the shot-to-shot fluctuation, the intensity of the analyte peak is normalized by the line intensity of an element from the matrix [43]. This procedure is called internal standardization.

While choosing the peak for normalization, the same protocol should be followed as given in 2.5.3. In addition, the difference in energy of the upper level of the analyte and the normalizing

peaks should be small compared to k_BT so that the effect of temperature fluctuations is minimized, as inferred by equation (45):

$$\frac{I_{ji}^{a}}{I_{kl}^{M}} \propto \frac{N_a^z}{N_M^z} \frac{U_M^z(T)}{U_a^z(T)} e^{-\frac{E_j - E_k}{k_B T}} \tag{45}$$

While designing the LIBS apparatus and formulating the experimental protocol, the facts stated in Sections 2.3 through 2.5 should be taken into consideration. The characteristics of the LIBS apparatus that allows for control of different variables mentioned in section 2.5 is given in the chapter four.

CHAPTER THREE: SIMULATIO OF YAG PLASMA FORMED IN AIR

As stated in section 2.4, a calibration curve is needed to find the stoichiometry shift in YAG samples. To this end, the intensity ratio of aluminum and yttrium lines are plotted against their molar ratio as shown in figure 9

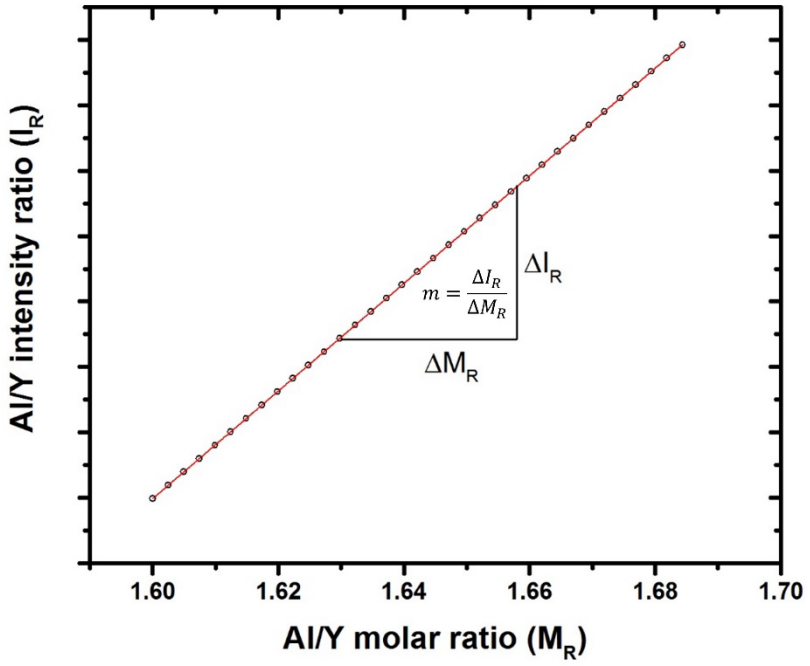


Figure 9. Hypothetical calibration curve to find the Al/Y molar ratio in YAG samples.

If the slope and intercept of the calibration curve are *m* and *c* respectively, the molar ratio of test sample is calculated by applying the following formula:

$$M_R = \frac{I_R - c}{m} \tag{46}$$

Here M_R and I_R are the molar and intensity ratios respectively.

If the standard deviation of intensity ratio is σ_{I_R}, the error in the corresponding molar ratio is:

$$\sigma_{M_R} = \frac{I_R - c}{m}\sqrt{\left[\frac{\sigma_{I_R - c}}{I_R - c}\right]^2 + \left[\frac{\sigma_m}{m}\right]^2} \quad (47)$$

Assuming that the relative errors in *m* and *c* are small compared to the relative error in I_R, equation 47 can be written as:

$$\sigma_{M_R} = \frac{\sigma_{I_R}}{m} \quad (48)$$

To differentiate the molar ratios between two adjacent points in x-axis of figure 9 with 99% confidence, $3\sigma_{M_R} < \frac{1}{2}\Delta M_R$ where ΔM_R is the smallest of the difference in molar ratios between adjacent samples. This implies that:

$$m > \frac{6\sigma_{I_R}}{\Delta M_R} \quad (49)$$

This expression shows that large sensitivity of the calibration curve is essential to accurately discern the molar ratios in YAG samples. For instance, the difference in molar ratio of the samples in the extremities of the solid solubility limit (section 1.3.1) is 0.03. The maximum standard deviation in intensity ratios that can be tolerated to differentiate these two samples is:

$$\sigma_{I_R} = m \times 5.4 \times 10^{-3} \quad (50)$$

Equation 45 shows that the ratio of emission line intensities depends on plasma temperature but how this ratio varies with it is not obvious. The change in sensitivity of the calibration curve with temperature cannot be foreseen either. The purpose of this chapter is to simulate the calibration curve at different plasma temperatures. The result of this calculation will help to obtain proper experimental protocol leading to the best sensitivity.

3.1 Calculations

Since the intensities of the emission lines at a given temperature depend on number densities of the emitters, the concentration of different atomic and molecular species as a function of temperature needs to be computed first. The plasma consists of ablated material vapor blended with the background gas. Let n_{vap} and n_{gas} be the atomic number densities of the ablated element (A) and the background gas (B) respectively. These elements exists as atoms (A^0, A^+, A^{++}, A^{+++}, B^0, B^+,B^{++},B^{+++}), homonuclear molecules (A_2, B_2, A_2^+,B_2^+) and heteronuclear molecules (AB, AB^+). At temperatures above 3000K, formation of polyatomic molecules can be neglected [94, 95] so that:

$$n_{vap} = n_A + \sum_{z=0}^{1} n_{AB}^z$$

$$n_{gas} = n_B + \sum_{z=0}^{1} n_{AB}^z \quad (51)$$

Where n_A and n_B are the number densities of element *A* and *B* excluding the molecule *AB* and equal to:

$$n_X = \sum_{z=0}^{3} n_X^z + \sum_{z=0}^{1} n_{X_2}^z \, , X = A, B \quad (52)$$

Ionization states up to +3 and +1 are considered for atoms and molecules respectively.

Assuming that the plasma is in local thermodynamic equilibrium (LTE), the number densities of ionic species can be obtained from the Saha equation (equation 10) combined with conservation of mass. It is to be noted, however, that the ionization energies are lowered in plasma due to presence of a micro electrostatic field and this reduction in energy can be well approximated using Unsöld's formula [96]:

$$\Delta E_z^{ion} = 3e^2(z+1)^{3/2}\left(\frac{4\pi}{3}n_e\right)^{1/3} \quad (53)$$

Number densities of neutral molecules are calculated using the law of mass action for chemical equilibrium [97]:

$$\frac{n_A^0 n_B^0}{n_{AB}^0} = \left(\frac{2\pi k_B T}{h^2}\frac{m_A m_B}{m_{AB}}\right)^{3/2}\frac{U_A^0 U_B^0}{U_{AB}^0}e^{-\frac{E_D}{k_B T}} \quad (54)$$

Here U_{AB}^0 is the partition function of a neutral molecule, E_D the molecular dissociation energy and m_A the mass of element A. The partition function of atomic species is given by:

$$U_A^z = \sum_j g_j e^{\frac{-E_j}{k_B T}} \quad (55)$$

Here, g_j is the degeneracy of energy level E_j. The atomic energy levels and their degeneracies can be found in NIST atomic level database [83]. Molecular partition function is calculated using the following expression:

$$\sum_{e,\vartheta,J}(2-\delta_\Lambda)(2S+1)e^{-\beta E_e}\times e^{-\beta E_\vartheta^e}\times g_N e^{-\beta E_J^{e,\vartheta}} \quad (56)$$

Here e, ϑ, and J are the electronic level, vibration quantum number and rotational quantum number respectively. The E's are the corresponding energies. δ_Λ is the Λ-type doubling factor and g_N is the nuclear statistical weight. The vibrational and rotational energies are given by:

$$E_\vartheta^e = hcG^e(\vartheta),\ G^e(\vartheta)=\omega_e\left(\vartheta+\frac{1}{2}\right)-\omega_e x_e\left(\vartheta+\frac{1}{2}\right)^2+\omega_e y_e\left(\vartheta+\frac{1}{2}\right)^3 \quad (57)$$

$$E_J^e = hcF_J^\vartheta(\vartheta),\ F_J^\vartheta(\vartheta)=B_\vartheta J(J+1)-D_\vartheta J^2(J+1)^2 \quad (58)$$

With $B_\vartheta = B_e - \alpha_e\left(\vartheta + \frac{1}{2}\right) + \gamma_e\left(\vartheta + \frac{1}{2}\right)^2$ and D_ϑ=$D_e - ß_e\left(\vartheta + \frac{1}{2}\right)$

The second and third order terms in equations (57)

and (58) arises because of anharmonic oscillations and deformable bonds. Values of the constants $\omega_e, \omega_e x_e, \omega_e y_e, B_e, \alpha_e, \gamma_e, D_e$ and $ß_e$ can be found in NIST chemistry web book [98].

The composition of the LIBS plasma at a particular temperature can be calculated using the algorithm given in [99] and outlined in figure 10.

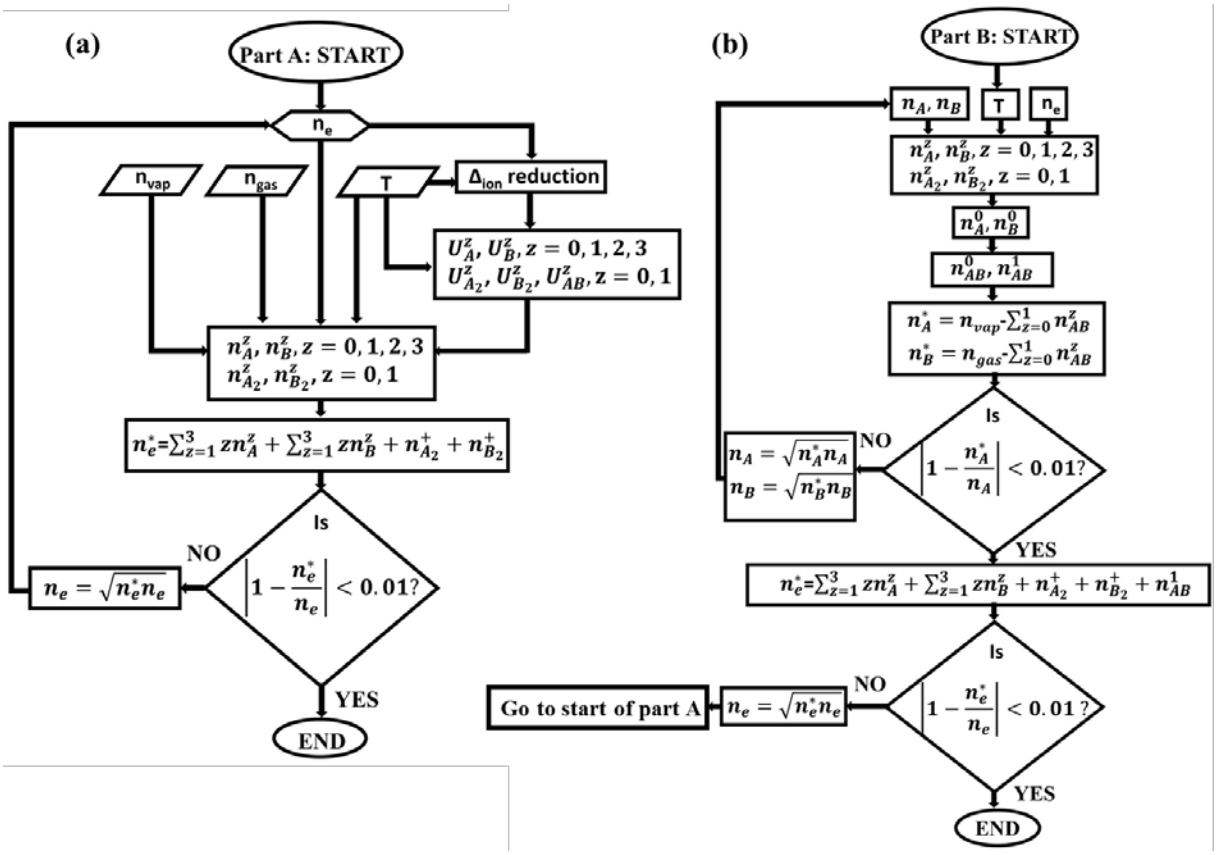


Figure 10. Algorithm flowchart for calculating number densities of different species in a plasma at local thermodynamic equilibrium. (a) Iteration loop to calculate ionization equilibrium and (b) chemical equilibrium.

The simulation is carried out using two iteration loops. The first loop is initialized with a certain electron number density n_e. Reduction in ionization potential is calculated based on equation 53 and then the partition functions are computed. Using these values, the number densities of neutral and charged atoms and homoneulear molecules are calculated. In the first part of the simulation, the material vapor and the background gas are not allowed to react so that $n_{vap} = n_A$ and $n_{gas} = n_B$. The electron density is given by:

$$n_e^* = \sum_{z=1}^{3} z n_A^z + \sum_{z=1}^{3} z n_B^z + n_{A_2}^+ + n_{B_2}^+ \quad (59)$$

If n_e^* and n_e differ by more than a percent, the value of n_e is updated as shown in figure 10 (a) and the calculation is repeated. After this loop converges, second iteration is initiated in which neutral species of elements A and B are allowed to react to form neutral AB. After computing the values of n_{AB}^0 and n_{AB}^+, the total number density of unreacted A and B are updated using equation 51:

$$n_A^* = n_{vap} - \sum_{z=0}^{1} n_{AB}^z$$

$$n_B^* = n_{gas} - \sum_{z=0}^{1} n_{AB}^z$$

Just as in charge equilibrium loop, if n_A^* and n_A differ by more than a percent, value of n_A is updated as shown in figure 10(b) and the iteration is restarted. After convergence, the electron number density is recalculated with the addition of the electrons coming from AB^+ species:

$$n_e^* = \sum_{z=1}^{3} z n_A^z + \sum_{z=1}^{3} z n_B^z + n_{A_2}^+ + n_{B_2}^+ + n_{AB}^+$$

Again, if the charge densities n_e^* and n_e differ by more than a percent, n_e is updated as

before and the computation is started right from the beginning of the first loop else the computation is stopped and the number densities are returned.

3.2 Results and discussion

The code for the simulation is written in MATLAB and its validity was tested by replicating the simulation results of Hermann *et al* [99]. The first trial was to simulate an aluminum plasma in an oxygen background. The starting values of n_{vap},and n_{gas} was set just as in the reference, i.e. 1×10^{22} m^{-3} and 1.1×10^{22} m^{-3} respectively. The result in the temperature range 4000 to 12000 K is shown in figure 11 and illustrates that our results (solid lines) are in excellent agreement with the results from the reference (circles). The results for an aluminum plasma in nitrogen, also a replication of the simulation from the same reference, is shown in figure 12 which further validates our procedure. The slight discrepancy in the number densities of nitrogen molecules in figure 12 may be due to omission of Λ-type doubling factor and nuclear statistical weight. Apart from this small difference, atomic number densities, which dictate the emission spectrum of LIBS plasma, are in very good agreement.

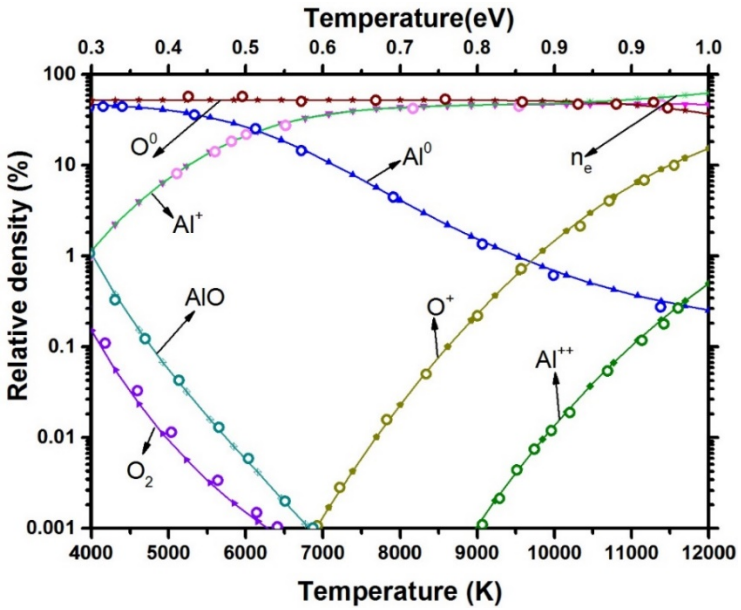


Figure 11. Number densities of plasma species as a function of temperature computed for aluminum. Circles are the simulation by Hermann *et al* [99] and the solid lines are our result. The number density of each species was normalized by the sum $n_{vap}+ n_{gas}$.

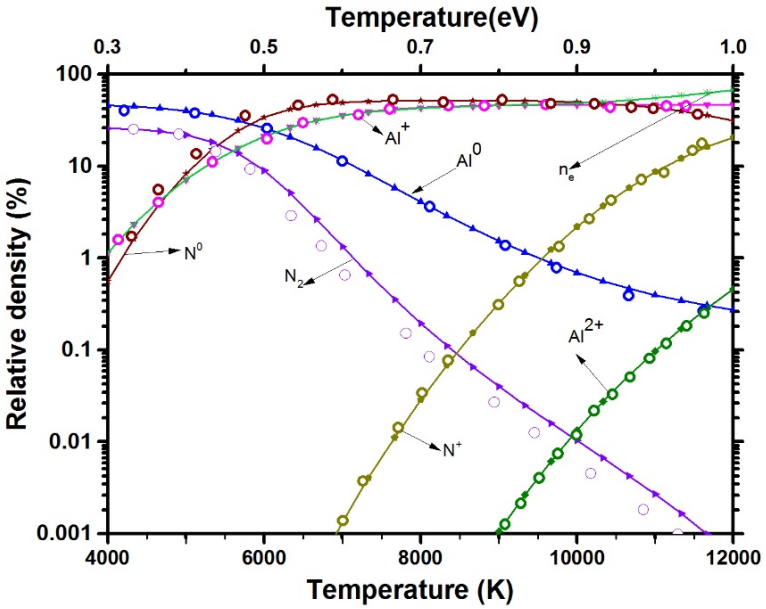


Figure 12. Simulation of aluminum plasma in nitrogen background. Circles are the results from [99] and the solid lines are our result.

After the validation of the simulation code, composition of YAG plasma in air was determined using the same algorithm. The number of moles of YAG ablated from the sample was calculated based on the experimentally observed crater size. The diameter of the crater on the surface of YAG samples was 100 μm, which is shown in chapter five. Assuming that all the ablated mass from the 100 μm diameter hemispheric crater goes into the plasma, the number density of YAG formula units ($Y_3Al_5O_{12}$) in the plasma will be 1.71×10^{23} m^{-3}. This corresponds to $5\times1.71\times10^{23}$ aluminum atoms, $3\times1.71\times10^{23}$ yttrium atoms and $12\times1.71\times10^{23}$ oxygen atoms per meter cube. Plasma diameter of 3 mm was assumed based on which the number density of oxygen and nitrogen atoms contributed by air enclosed in a sphere of 3 mm diameter was calculated. Setting the pressure to 1 atm, temperature to 300 K and nitrogen to oxygen ratio to 3.7, ideal gas law was applied to this sphere resulting in 1.08×10^{25} m^{-3} oxygen atoms and 3.8×10^{25} m^{-3} nitrogen atoms. Electron density of 1.5×10^{23} m^{-3} was taken to initialize the simulation. The variation of number densities of different species in the temperature range 5500 K to 18000 K is shown in figure 13.

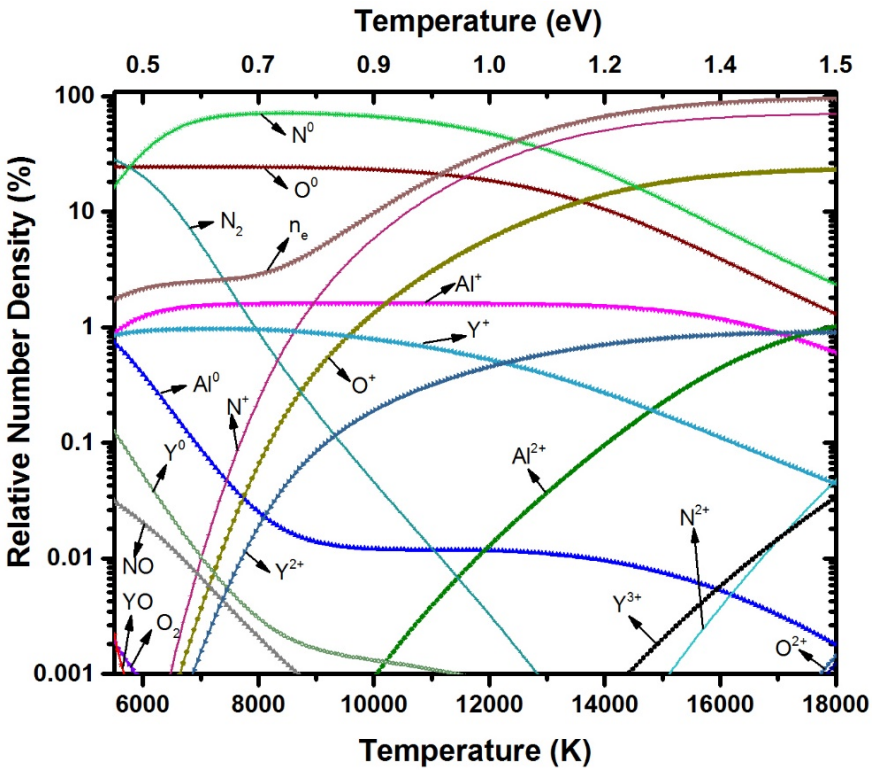


Figure 13. Simulation of YAG plasma in air. The number density of ablated YAG molecules was estimated to be 1.71×10^{23} m^{-3} based on the experimentally observed crater size. The air pressure was set to 1.01×10^{5} Pa and the ratio of nitrogen to oxygen atoms was set to 3.7 to simulate the atmospheric condition.

From figure 13 it can be inferred that above 10000 K, electron number density follows the trend of N^+. The neutral atomic species Y^0 and Al^0 varies rapidly with temperature up to 8000 K. Al^0 levels off after this temperature while Y^0 becomes vanishingly small. On the contrary, the singly charged species Al^+ and Y^+ are relatively stable with temperature. This trend suggests that emission lines from Al^+ and Y^+ should be chosen for analysis so that shot-to-shot fluctuation in plasma temperature will have minimal influence on the intensity ratio. Because of the close proximity of the upper energy levels, Al 281.61 nm and Y 278.52 nm lines were chosen to see the behavior of Al/Y intensity ratio with temperature (figure 14).

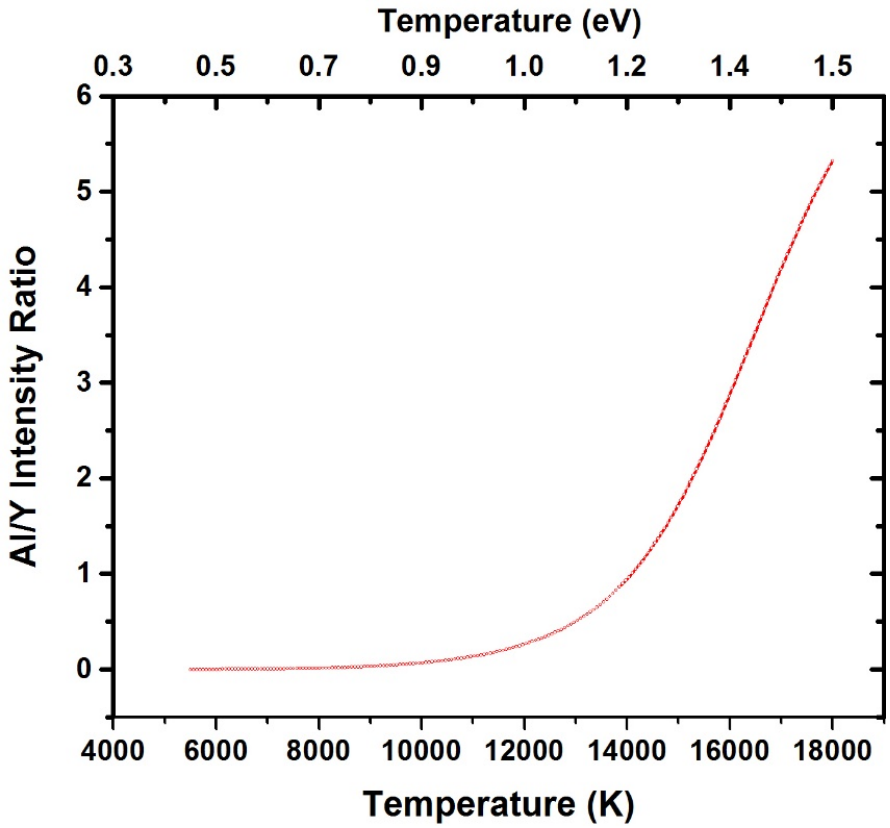


Figure 14. Simulated Al/Y intensity ratio as function of plasma temperature. Al 281.61 nm and Y 278.52 nm peaks were used for this purpose.

The intensities was calculated using equation 8 and the values of A_{ji} , g_j and λ_{ji} were extracted from Kurucz database [100]. The ratio increases sharply after 12000 K which suggests that above this temperature, a tiny fluctuation in plasma temperature can produce large variation in the intensity ratio. However, this does not elucidate the behavior of sensitivity with temperature.

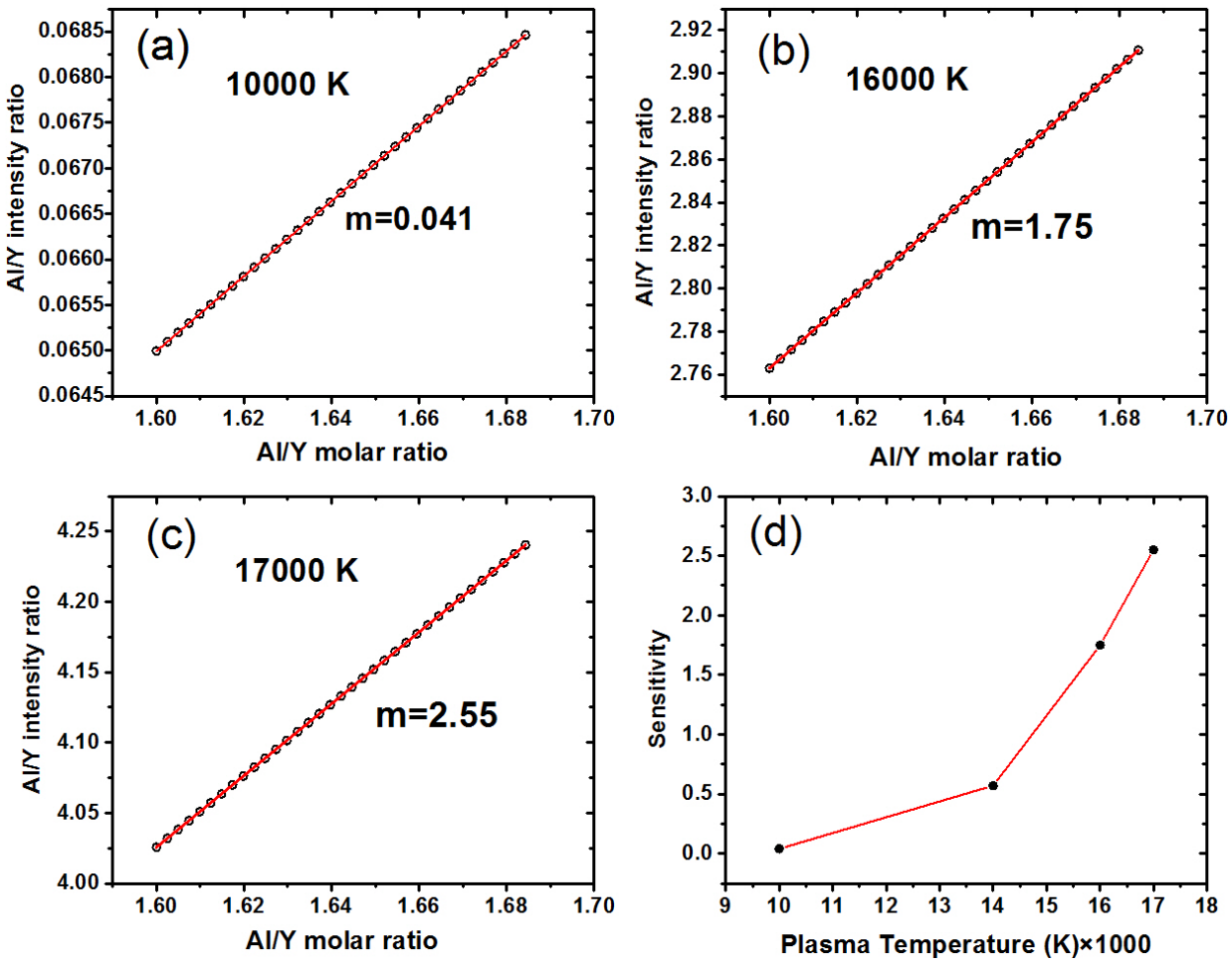


Figure 15. Sensitivities of the simulated calibration curves. The results show that the sensitivity increases sharply after 14000 K.

To this end, a simulation was performed at four different temperatures. At each temperature the molar ratio of Al/Y was varied from 1.6 to 1.68 with a step size of 0.0025. The results show that the sensitivity rapidly increases above 14000 K. Though the result from figure 14 suggest that effect of shot-to-shot temperature fluctuation is insignificant below 12000 K, the molar ratios are too small to be resolve experimentally. ***If the parameters discussed in chapter 2 are properly***

controlled, higher plasma temperature are found to be better resolve tiny variation in molar ratios (equation 49).

3.3 Conclusion

In this chapter, the composition of YAG plasma was calculated by iterative simulation. The results show that the Al/Y molar ratio varies sharply above 12000 K implying that experiments should target plasma temperatures below this value so that its shot-to-shot fluctuations has minimal effect in the intensity ratio. On the other hand, simulated calibration curve at different temperatures show that the sensitivity increases from 0.04 to 2.6 when the temperature is increased from 10000 K to 17000 K. Also, at lower temperatures, the intensity ratios are too small to be experimentally resolved. It was also shown that to differentiate the molar ratio, ΔM_R, with 99% confindence, the sensitiivty should be greater than $\frac{6\sigma_{I_R}}{\Delta M_R}$. All these facts guides towards higher plasma temperature for greater senistiviy while maintaining tight control in the experimental parameters so that the standard deviaiton in intensity ratio is smaller than m× ΔM_R.

CHAPTER FOUR: QUANTIFICATION OF NONSTOICHIOMERY IN YAG

Based on the trends highlighted in Chapter 3, we aim at experimentally validating the possibility of measuring slight changes in composition near the YAG stoichiometric ratio in sintered ceramics of Al_2O_3-Y_2O_3 mixtures. Besides the proof-of-concept of such a sensitive quantitative analysis on major analytes, we are interested in establishing (i) if enough sensitivity can be achieve to resolve the width of the garnet solid-solution, as determined by prior optical microscopy and XRD experiments, and (ii) a protocol for this analysis[5].

4.1 Fabrication of ceramics with varied compositions near the garnet phase

To carry out this study, yttrium aluminum oxide ceramic samples of varied compositions near the garnet stoichiometry were prepared by solid-state reaction between alumina and yttria [12]. A 50 g powder mixture of 38 mol% α-Al_2O_3 (Inframat) and 62 mol% Y_2O_3 (Inframat) was ball-milled for 8 hours in the presence of ethanol and alumina balls as a grinding medium. Tetraethoxysilane (Sigma Aldrich) was added to the slurry at a concentration of 0.5 wt % as a sintering additive. After drying, 4 g aliquots of this mixture were blended with controlled quantities of Y_2O_3 to prepare pellets of known composition. Fourteen such samples were prepared with Al/Y molar ratio ranging from 1.600 to 1.684, with step size no more than 0.007. The ratio of 1.667 corresponds to stoichiometric YAG. The degree of hydration of the raw powders and imprecision of the weighing scale (0.2 mg) both contributed to composition uncertainties. The weight loss of

[5] These results have been published in Pandey, S. J., Martinez, M., Pelascini, F., Motto-Ros, V., Baudelet, M., & Gaume, R. M. "Quantification of non-stoichiometry in YAG ceramics using laser-induced breakdown spectroscopy". Optical Materials Express, 7(2), 627-632.

the raw powders after calcination at high temperature was determined and accounted for in the fabrication of the ceramic samples. The cumulated error amounted to 0.02% of the nominal compositions (i.e. an order of magnitude smaller than the composition increments between samples). The powder samples were then uniaxially pressed at 20 MPa into pellets and cold isostatically pressed at 200 MPa. After compaction, the pellets were vacuum-sintered in a tungsten-mesh furnace at 1750°C at a pressure of 10^{-6} torr for 2 hours and hot-isostatically pressed at 1700°C at 200 MPa for 2 hours. The samples were subsequently annealed in air at 1400°C for 3 hours. To prevent secondary phase precipitation, cooling rates were maintained above 15°C per minute. Samples within $1.635<Al/Y<1.669$ are transparent but translucent outside this composition range.

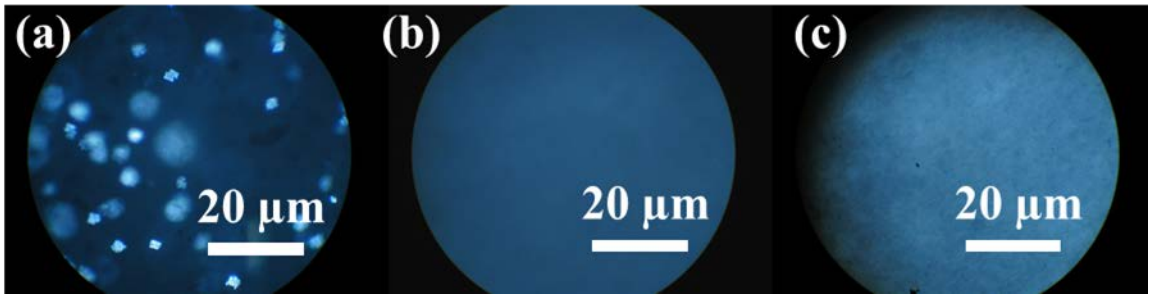


Figure 16. Optical microscopy images of YAG samples. (a) Al/Y molar ratio=1.673. The bright spots are due to light scattering from Al_2O_3 precipitates (b) Transparent sample with Al/Y molar ratio=1.667 (stoichiometric YAG) and (c) Translucent sample with Al/Y molar ratio=1.6213

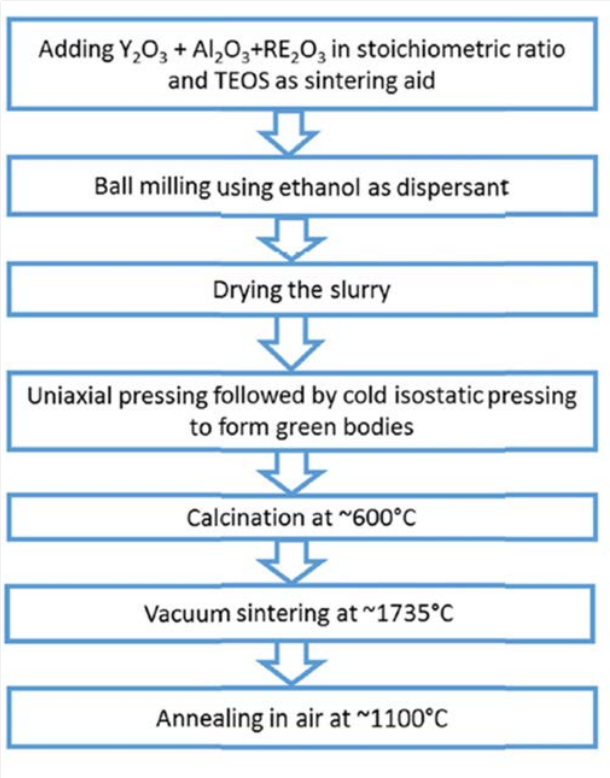


Figure 17. Flowchart depicting the fabrication process of YAG ceramics.

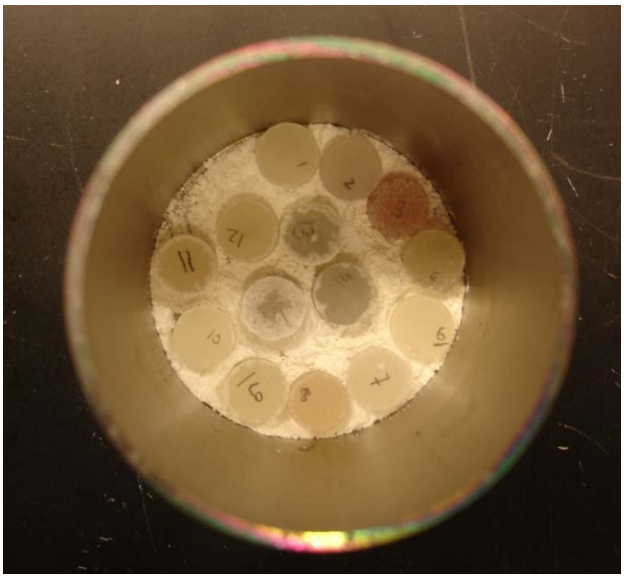


Figure 18. Ceramic samples after vacuum sintering. Each sample is ¼" in diameter. YAG powder was laid at the bottom of the tungsten crucible to prevent sticking. Note the reddish-

brown color of alumina-rich samples. The color goes away after annealing. At this stage of the process, the roughness of the surface prevents seeing the actual transparency of the samples.

4.2 LIBS analysis for the quantification of stoichiometry

The laser ablation was carried out at the fourth harmonic of a Q-switched Nd:YAG laser (266 nm, 10 mJ, 5 ns, 10 Hz, Quantel). The laser pulse energy was optimized to produce a stable plasma and maximum ablation for increasing the signal-to-noise ratio and reducing the effect of possible sample heterogeneity. The LIBS apparatus was configured as shown in figure 19.

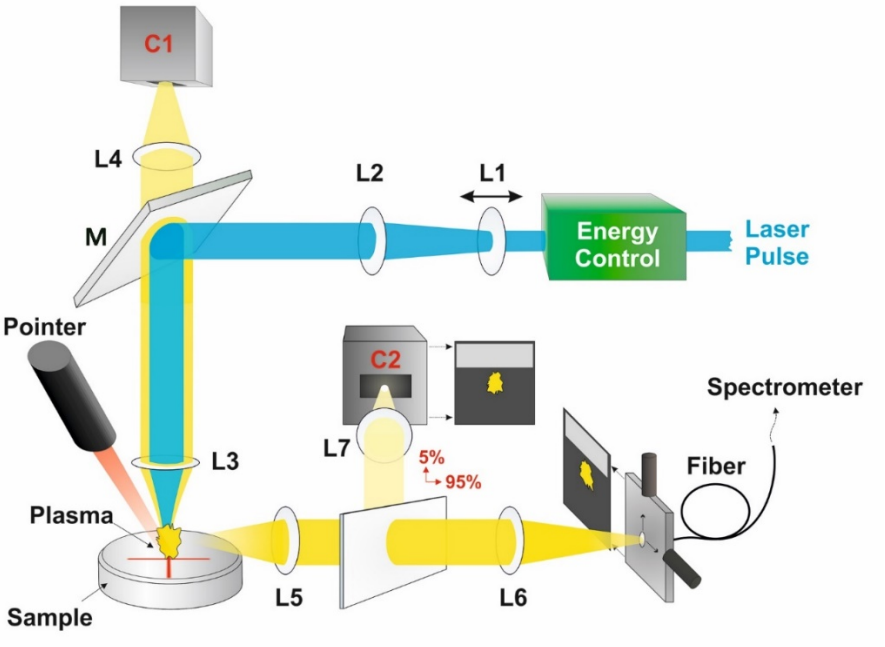


Figure 19. Configuration of LIBS system used in this study

The laser energy is stabilized during the experiments using a combination of a power-meter and a computer controlled attenuator (ATT266 from Quantum Composers). The laser beam is

expanded by lenses L1 and L2, with focal lengths of -50 and 100 mm, respectively (Fig. 1). It is then reflected off mirror M towards the converging lens L3 (focal length 75 mm). Lenses L1, L2 and L3 are made of fused silica and the dielectric mirror M has a high reflectance at 266 nm and a high transmittance for wavelengths above 300 nm. The beam is focused few hundreds of micrometers under the sample surface which is necessary to prevent air breakdown and produce a stable plasma [85]. The focus point of the laser can be adjusted in height by translating lens L1 horizontally with a motorized translation stage. The ability to control the distance between lens L3 and the sample surface is an important feature of the present system, which guarantees the production of identical fluences and plasma conditions from sample to sample. A laser pointer is directed towards the sample in an oblique fashion and the light reflected off the sample surface is focused by lens L4 onto the CCD camera C1. In the field of view of the camera, the barycenter of the laser spot is very sensitive to the vertical positioning of the sample surface and allows for locking the lens-to-sample distance with an accuracy better than 5 μm. This technique is detailed in [85]. The plasma light is collected by lens L5 of 5 cm focal length and fed into a Czerny-Turner spectrometer (1200 1/mm grating) via an optical fiber consisting of a bundle of 19 fibers of 200 μm core diameter each. The stability of the plasma is monitored by the CCD camera C2 (Thorlab) and the collection fiber is centered with respect to the plasma to account for the shot-to-shot fluctuation of plasma morphology. An intensified charge coupled device (ICCD) camera (Andor Technology) is used for recording the spectra. In this experiment, delay for the laser pulse and the duration of acquisition by the ICCD camera were set to 900 and 1000 ns, respectively.

As discussed in 2.1.2, the quantification of major elements by atomic spectroscopy techniques is hampered by self-absorption [101, 102], and the non-resonant lines of singly-ionized

aluminum (281.61 nm) and yttrium (278.52 nm) were chosen for this analysis [103]. These lines are well isolated and do not suffer any spectral interference. The typical emission spectrum produced by an yttrium aluminum oxide sample, in the 274 to 290 nm spectral window, is shown in Fig. 15. For each sample, 100 spectra were averaged over a 10x10 spot grid to decrease the variance of the measurement and overcome a possible sample heterogeneity. Each individual spectrum was recorded with the accumulation of 10 laser shots at the same position. With this protocol, the duration of a measurement sequence of 100 spectra for a sample was less than 2 minutes. The center to center spacing between neighboring craters was 300 μm. A typical LIBS spectrum from YAG is shown in figure 20.

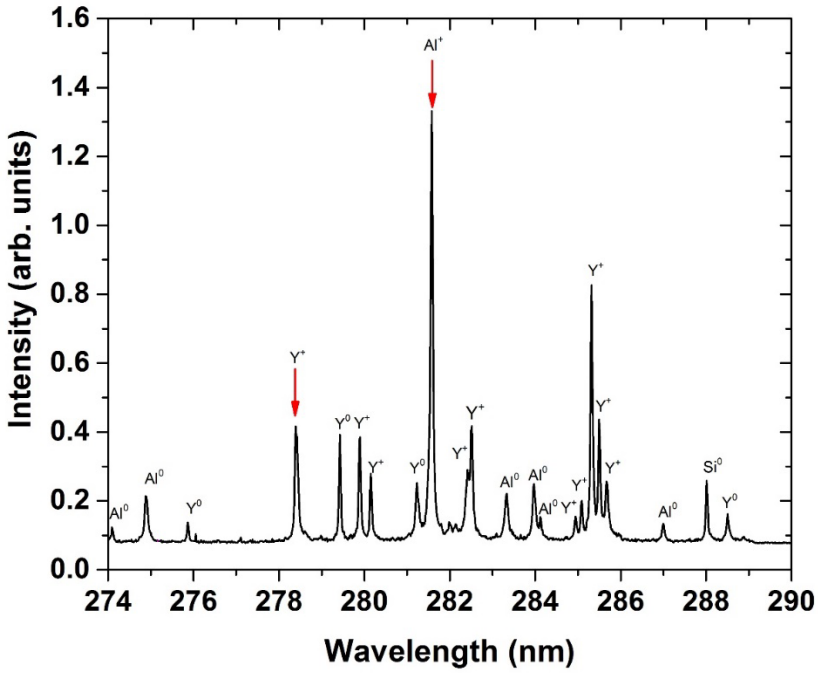


Figure 20. Typical LIBS spectrum of an yttrium aluminum oxide sample, showing the Al^+ and Y^+ lines used for quantitative analysis. The other spectral features correspond to transitions in neutral and ionized Al and Y species.

4.3 Results and discussion

Figure 21 shows the correlation between the sample composition and the intensity ratio of the 281.61 nm aluminum and 278.52 nm yttrium lines. The calibration curve has three separate trends that correlate to the transparency of the samples. The relationship between the Al/Y intensity and molar ratios is monotonic irrespective of the visual appearance of the samples. The sensitivity of the calibration curve in group I, II and III is 4.31±1.4, 1.53±0.09 and 3.09±0.78, respectively. This correlation is likely due to differences in laser-sample interaction brought about by light-scattering from secondary phases (Al_2O_3 or $YAlO_3$) outside the garnet solid-solution (i.e. outside of group II). As discussed above, the small magnitude of the error bars on the composition axis does not show on the graph. The measured shot-to-shot fluctuations of the Al and Y lines over 1000 spectra is 1%. The propagation of this error into the Al/Y intensity ratio, *r*, and obtained from:

$$\frac{\Delta r}{r}=\left[\left(\frac{\Delta I_{Al}}{I_{Al}}\right)^2+\left(\frac{\Delta I_{Y}}{I_{Y}}\right)^2\right]^{1/2} \tag{60}$$

where I_{Al} and I_Y designate the line intensities of both Al and Y species, leads to a 1% relative standard deviation on the Al/Y intensity ratio. ***This allows resolving a 0.3 mol% difference in the Al/Y molar ratio for group II samples, and these calibration curves can be used for determination of composition in yttrium aluminum oxide ceramics on either side of the garnet stoichiometric composition.***

We believe that such performance will allow better composition control in the fabrication of advanced ceramics of definite line-compounds, particularly that of high-grade transparent ceramics.

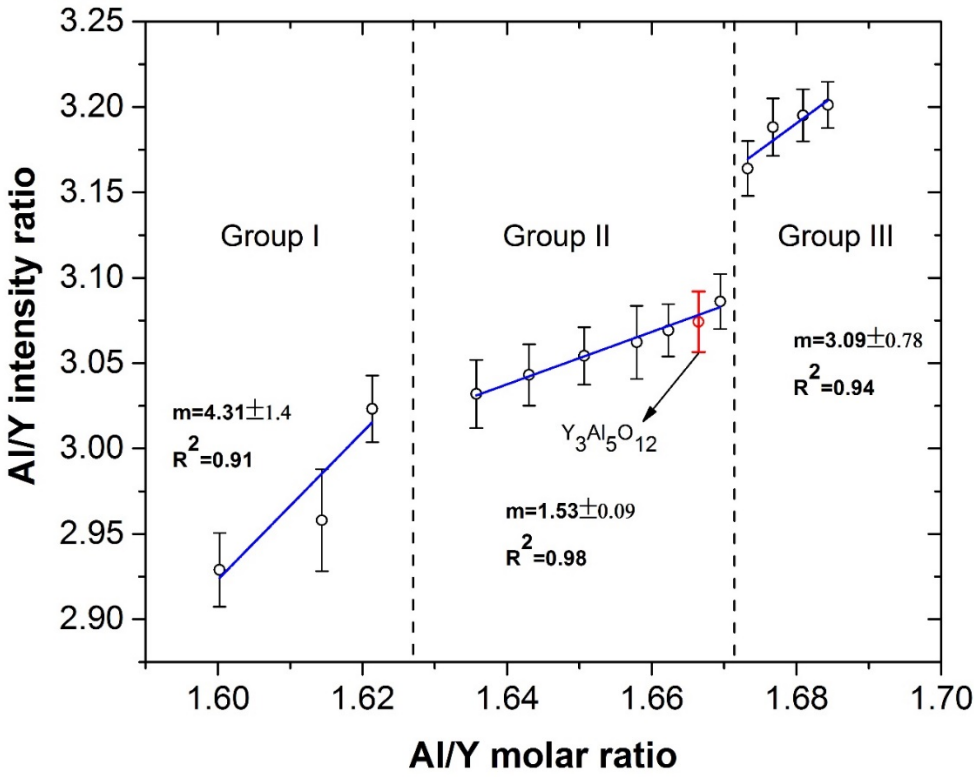


Figure 21. Variation of the 281.61 nm aluminum and 278.52 nm yttrium line intensity ratios with sample composition. The arrow points to the sample with the stoichiometric garnet phase composition (YAG). The 3 domains (labeled group I, II and III) correspond to the visible appearance of the samples: transparent for group II and translucent for groups I and III. The changes in slope, *m*, seen in the calibration curves between these groups reflect differences in laser-sample interaction.

However, the absolute value of the standard deviation for the intensity ratios of group II is 0.02. Equation 49 reveals that the sensitivity of the calibration curve for group II can be used to determine the molar ratio of test samples with 99% certainty only if the error bars are reduced by an order of magnitude. Several ways can be explored to reduce these fluctuations further and achieve this value. For example, the intensity ratios were calculated by taking the ratios of the peak

height but as explained in chapter 2, the area under the peaks should be used to increase the accuracy of intensity measurements. Also, the peaks can be normalized by a featureless background to reduce the shot-to-shot fluctuations. The green bodies were prepared by mixing the powders in a mortar for about 20 minutes which may not be enough for homogeneous blending. A more homogenous sample would lead to less shot-to-shot fluctuations. The procedure for maintaining constant lens-to-sample distance used in this study does not work well for transparent samples which demands for more elaborate techniques. The plasma temperature was not measured in this particular experiment. A more detailed experiment to obtain calibration curves at different temperatures is needed to optimize the sensitivity and the intensity fluctuations and achieve the desired resolution.

CHAPTER FIVE: STUDY OF THE EFFECT OF POWDER COMPACT DENSITY ON LIBS ANALYSIS OF MINOR ELEMENT

In chapters 4, the quantification of the stoichiometry shift was performed on sintered ceramics. For the quick feedback on the correctness of the stoichiometry it would be better if the shift can be measured right after powder mixing. But the shot-to-shot fluctuation of LIBS signal may occur due to the inhomogeneity of powder surface density. To test the feasibility of such measurement, the behavior of the calibration curve of minor element spiked in alumina was monitored for different powder-compact density and particle size[6].

5.1 Sample preparation

Three different varieties of α-alumina powders was used in this study and are labelled S1, S2 and S3. Sample S1 (99.99% purity, Inframat® Advanced Material™) is composed of 190 ± 64 nm-sized particulates agglomerated into particles with average hydrodynamic diameter of 180 nm. Sample S2 (99.99% purity, Inframat® Advanced Material™) has a similar morphology, with ultimate particle size of 500 ± 160 nm and an average hydrodynamic diameter of 1.7 μm. The hydrodynamic size distribution, measured by ultrasound spectroscopy (Acoustosizer II, Colloidal Dynamics), shows that sample S1 has very few agglomerates whereas S2 has a very broad size distribution ranging from few tenth of nanometers to hundreds of micrometers. Sample S3 (99.9%, Alfa Aesar) has an average particle size of 35 ± 13 μm. SEM images of these samples are shown in figure 21. To prepare samples with varied nickel doping concentrations, 2.5 mg of nickel

[6] This work has been submitted to Pandey, S. J., Locke, R., Gaume, R.M and Baudelet, M. "Effect of powder compact density on the quantification of minor elements by LIBS". Spectrochimica Acta B, 2017.

chloride hexahydrate crystallites (Scientific Products, Irvine, California) was dissolved in 250 ml of deionized water and appropriate amount of this solution was added to 3-g aliquots of alumina powder. The mixture was homogenized in the presence of ethanol for 30 min in an alumina mortar, dried and pressed to the desired density in a stainless steel die. All the densities mentioned in this paper are given relative to that of fully dense alumina (3.95 g/cm^3). The concentration of nickel was varied from 500 to 3000 ppm, by 500 ppm increments. The densities of S1 and S2 were varied from 13% (loose powders) to 46%, and 16% to 43%, respectively while S3 had a single density value of 41% and could not be compacted further due to the coarseness of the alumina grains.

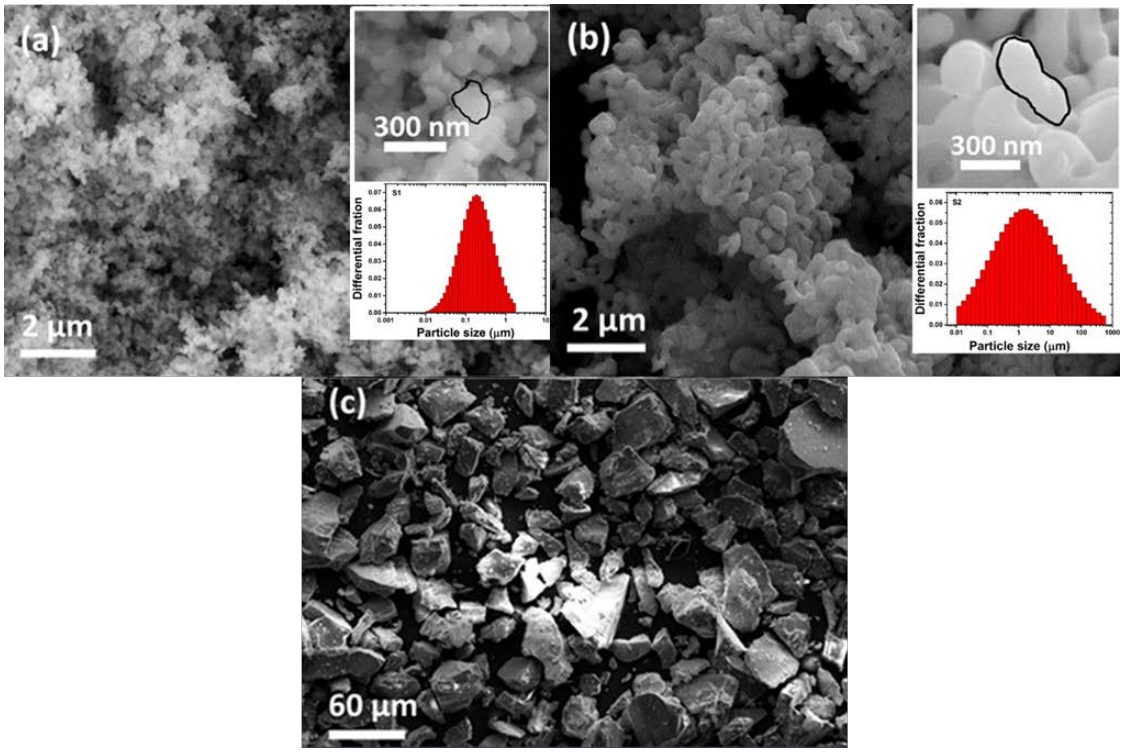


Figure 22. SEM images of alumina powders used in this study. The inset is the image taken at higher magnification and hydrodynamic size distribution. (a) Sample S1 (b) Sample S2 (c) Sample S3.

5.2 LIBS protocol

The LIBS setup used in this experiment has a similar configuration as the one used in chapter 4 and was built in-house. Q-switched Nd:YAG laser ((1064 nm, 5 ns, 10 Hz Quantel) is used as the ablation source. Princeton SpectraPro 2500i spectrometer (1200 grooves/mm, 0.1nm wavelength resolution) coupled with Andor iStar ICCD camera is used for recording the spectra. The spectral response calibration was carried out using calibrated deuterium lamp (Ocean Optics, DH-2000).

LIBS on loose powders were carried out by putting them in a 2.5-cm diameter and 1-cm deep sample holder made of copper. The powders were filled up to the brim of the holder and levelled with a microscope slide without pressing. The densities of the samples were measured by dividing their mass by volume. The measurement errors were 10% for loose powders and 1% for compact pellets. Spectra were collected by the accumulation of 3 shots from 65 randomly selected spots on the sample surface. In the case of loose powders, the sample holder was emptied and refilled after taking 20 measurements to present fresh surface for ablation. The ICCD detection gate delay and width were set at 900 ns and 2 µs respectively. The laser pulse energy was measured by an energy meter (Gentec Solo2) and set at 9 mJ. The relative standard deviation of pulse energy measured over 500 pulses was 0.5%. The ICCD settings and laser energy were optimized for maximum signal-to-noise ratio.

5.3 Results and discussion

A typical LIBS spectrum of nickel-spiked alumina sample is shown in figure 23. Calibration curves were built by normalizing the integrated intensity of the nickel peak at 301.2 nm ($3d^9(^2D)4s \leftarrow$

$3d^8(^3F)4s4p(^3P)$) by the sum of integrated aluminum peaks at 305.4 nm ($3s3p^2$4P1/2 ← $3s3p(^3P)4s^4P_{3/2}$) and 305.7 nm ($3s3p^2$4P$_{5/2}$ ← $3s3p(^3P)4s^4P_{5/2}$). The normalization was implemented after baseline correction.

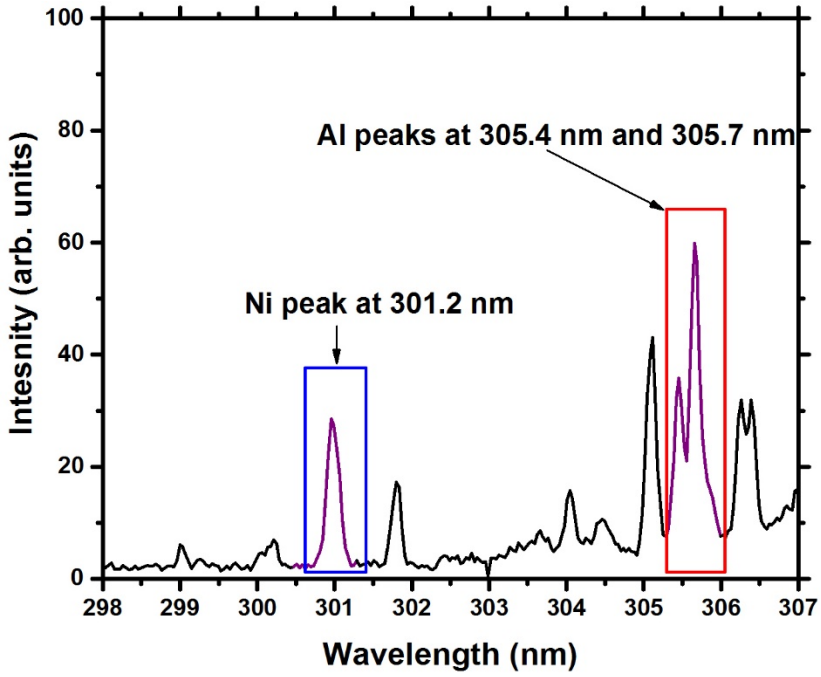


Figure 23. LIBS spectrum of nickel spiked alumina samples in between the wavelength limit 298 nm-307nm.

To find the optimum laser energy for the experiment, the behavior of the calibration curve was observed at 4, 6, 9 and 12 mJ, as shown in figure 24. The sensitivity, as well as the relative standard deviation of shot-to-shot fluctuations, decrease with increasing laser energy levels. The R^2-value of the linear fit also approaches unity as laser energy increases. The sensitivity and its standard deviation have similar values for 9 and 12 mJ and the former energy value was chosen for the rest of the experiments.

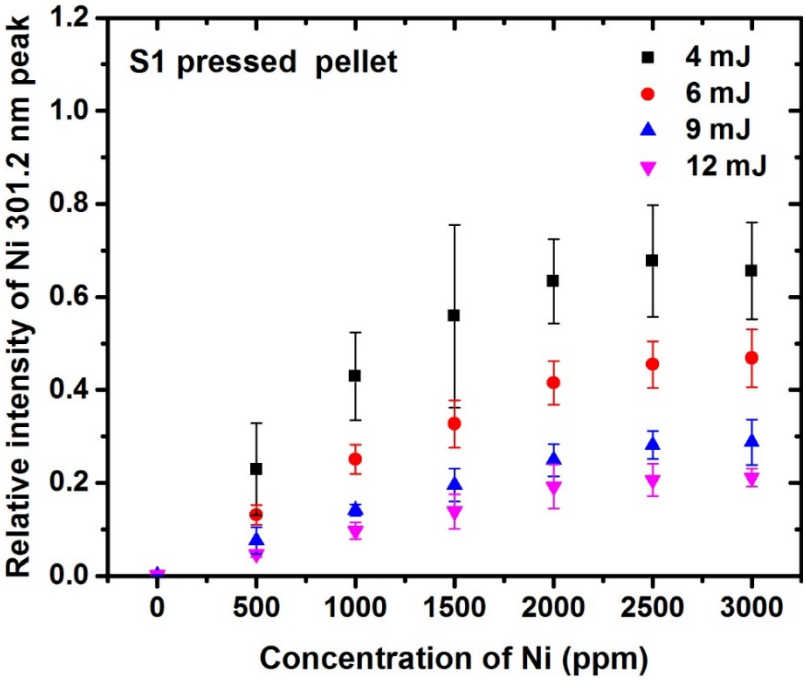


Figure 24. Calibration curve for different laser energies for pressed pellet of powder S1.

Figure 25 is the comparison between the LIBS spectra of S1, S2 and S3. Each spectrum is the average of 65 spectra on sample containing 2000 ppm of nickel. The intensity of S3 is an order of magnitude larger than that of S1 powder and pressed pellet. Sample S2 shows the same features as S1. This may well be due to larger scattering coefficient, governed by the ultimate particle sizes, for powders with smaller particles. In fact, Mie scattering calculations [104] at 1064 nm wavelength show that 200 nm particulates scatters the incoming laser beam near-isotopically and has a scattering coefficient two orders of magnitude larger than 30 μm particles. The difference in particle shape may also have led to disparity in laser-sample coupling. The particles of S3 are flat and on average, they provide more surface area for ablation. Further experiments need to be done to verify this hypothesis.

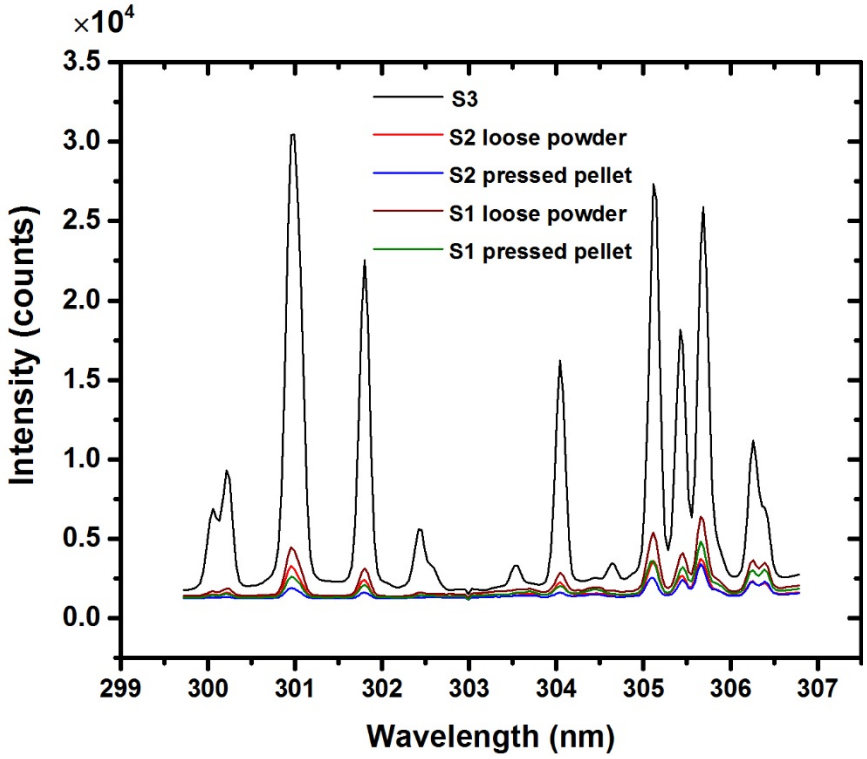


Figure 25. Comparison of spectra from S1, S2 and S3. Intensity from S3 is an order of magnitude higher than both S1 and S2 powders and pressed pellets.

It is to be noted that there are two nickel lines at 305.43 nm and 305.76 nm that can possibly interfere with aluminum lines at 305.47 nm and 305.71 nm respectively. To quantify the importance of this interference, the line intensities I_{ji} between upper and lower levels j and i of a given electronic transition, respectively, were simulated as a first approximation using equation (7) and (9). In this simulation, the molar ratio of nickel to aluminum was set at 1.4×10^{-3}, a value equivalent to 3000 ppm of nickel by weight. The parameters for the atomic lines were retrieved from the Kurucz database [100] and the atomic level data for the calculation of partition functions were retrieved from NIST atomic level database [105]. The intensities as a function of temperature in the range of 5000 to 20000 K is shown in figure 26. It can be clearly seen that at temperatures

greater than 10000 K, the aluminum line intensities are more than two orders of magnitude larger than those of nickel, which justifies that, in these conditions, any interference between these two species can be neglected.

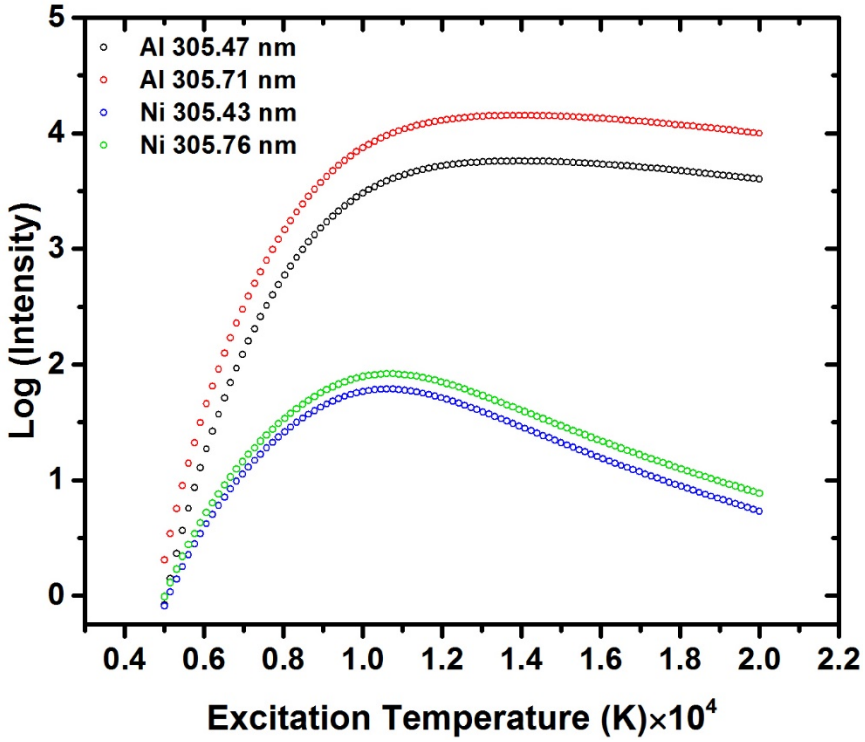


Figure 26. Simulated intensities of Al 305.47 nm, Al 305.71 nm, Ni 305.43 nm and Ni 305.76 nm peaks as a function of temperature.

The excitation temperature of aluminum for undoped samples was calculated for different powder compact densities using a Boltzmann plot as shown in figure 27. The aluminum peaks at 237.21 nm, 256.79 nm, 257.51 nm and 266.04 nm were used for this purpose. The laser pulse energy was set at 9 mJ. The spectral data was fitted with a pseudo-Voigt function to get the integrated intensities. The excitation temperature for a given sample was calculated by averaging over 60 spectra. A comparison of all the samples shows that the regardless of the density and particle size

differences, the excitation temperature remains nearly constant around 12600 K. Referring back to figure 23, this confirms the lack of any significant interference from nickel onto the aluminum peaks used for normalization.

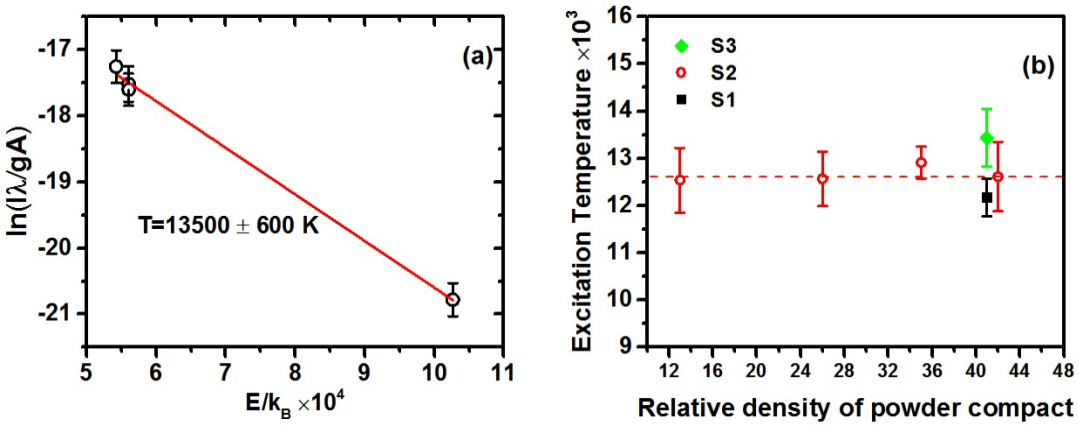


Figure 27. (a) Boltzmann plot for S3 (b) Variation of the excitation temperature of aluminum for various powder-compacts.

The calibration curves as a function of powder compaction densities for three samples are shown in figure 28. The shot-to-shot fluctuations in signal for samples S1 and S2 decrease significantly after compaction. The data points between 500 and 3000 ppm, which lie outside the shaded portion of figure 28, behaves linearly. The sensitivity was calculated by fitting a linear regression on this portion of the calibration curve. As expected from figure 25, both sensitivity and its standard deviation decrease with powder compaction, as shown in figure 29. The high relative standard deviation at lower densities may be due to dissimilar shot-to-shot ablation [106]. The loose powders are easy to eject, an effect which has been shown to cause intensity fluctuations in plasmas contaminated with micron-sized dust particles [107, 108]. This effect may not be the same for each ablation event. All particle sizes have same relative standard deviation for similar relative densities but the sensitivity of S3 is nearly twice as high as for S1 and S2. These results clearly indicate that

both the particle size and compaction impact the sensitivity and reproducibility of the calibration curve.

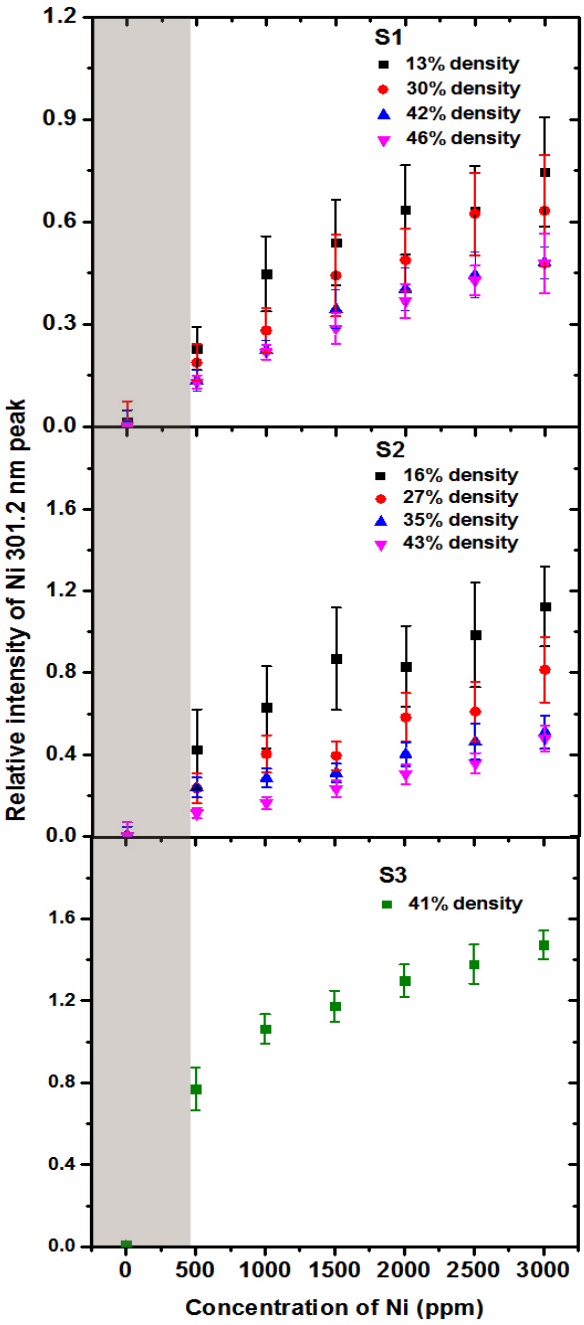


Figure 28. Calibration curve as a function of powder compaction and particle size. Large fluctuation in signal is observed at lower densities

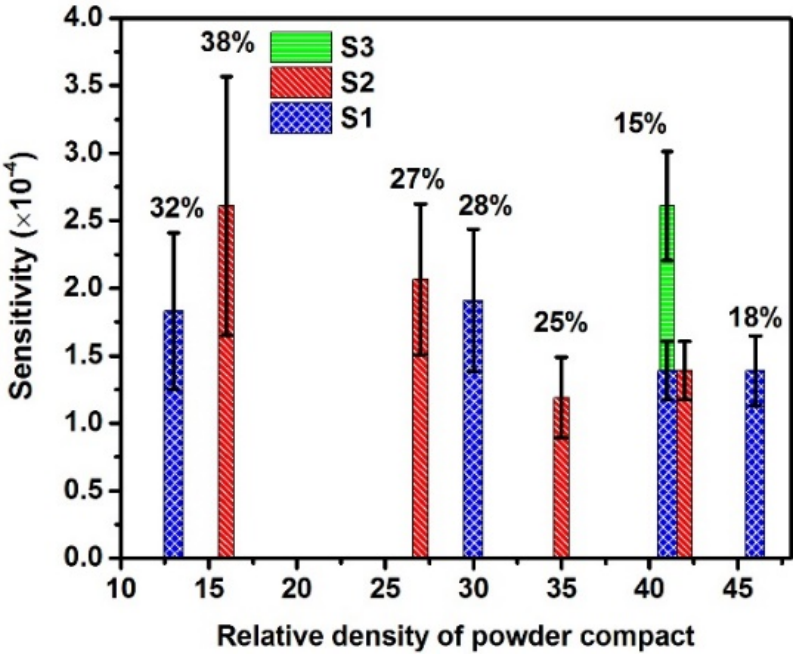


Figure 29. Variation of sensitivity with powder compaction. The numbers on top of the data points are the relative standard deviation values.

5.4 Conclusion

In this work, the effect of powder compact density on the calibration curve was studied to test the repeatability of LIBS measurements on powdery samples. To this end, alumina powders were spiked with nickel chloride in a 500 to 3000 ppm concentration range. It was observed that a stable LIBS signal can only be achieved after the powders are compacted to more than 40% relative density, and that the error in the sensitivity of the calibration curve is reduced to 15% by this procedure. However, the excitation temperature was unaffected by the powder particle size and density of the powder compact. Sample particle size also affects the sensitivity. Two hundred nanometers and 500 nm ultimate particle sized samples have the same sensitivity and relative standard deviation at similar densities but the value for 30 µm powders were twice as high. This suggest that the sample morphology should also be taken into consideration in calibration-based

quantification techniques. Also, it should be reminded that in the calibration curve presented in chapter 4, the standard deviation of each data point is less than 1%. This implies that LIBS measurement with an intent to discern stoichiometry shift in powder mixtures and powder compacts will not be reliable. The implication of this conclusion is far-reaching. Powdery samples, such as soil, are routinely analyzed by LIBS either as loose powder or pressed pellet. The elemental quantification in soil is made difficult by soil heterogeneity and matrix effect due to difference in chemical composition [91, 109], moisture level [92, 110], and/or particle size [56, 92]. Various multivariate data analysis techniques such as principal component analysis [53, 111], artificial neural network [53, 112] and support vector machines [113, 114] have been used to mitigate this problem. Yet, it is imperative to minimize the shot-to-shot fluctuations of LIBS spectra in order to accurately classify different soil types and quantify elemental composition [109]. The result of this chapter shows that the LIBS measurements on ceramic samples with particle size less than or close to a micrometer should be performed only after compaction.

CHAPTER SIX: QUANTIFICATION OF SiO_2 SINTERING ADDITIVE IN YAG

The LIBS measurement[7] was done on the samples at different stages of fabrication as depicted in figure 30. The samples were prepared following the protocol given in chapter four.

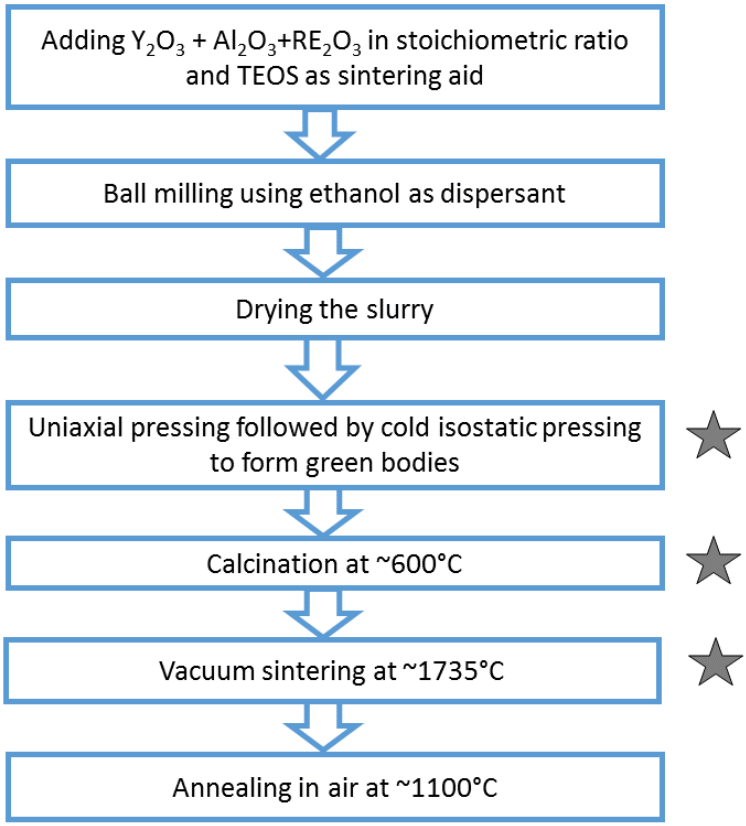


Figure 30. Flow chart for the fabrication of rare-earth (RE) doped YAG transparent ceramics. Samples for analysis were taken out at the steps marked by stars.

[7] These results have been published in Pandey, S. J., Martinez, M., Hostaša, J., Esposito, L., Baudelet, M., & Gaume, R. M. "Quantification of SiO2 Sintering Additive in YAG Transparent Ceramics by Laser-Induced Breakdown Spectroscopy (LIBS)". Optical Materials Express, 7(5), 1666-1671.

6.1 Sample preparation

High-purity aluminum oxide (Taimei, 4N, 0.2 μm) and yttrium oxide (Nanocerox, 4N, 0.05 μm) powders were mixed in stoichiometric amounts. The sintering additive was introduced to the blend in the form of SiO_2 powder, (99.99%, Sigma-Aldrich, USA) or TEOS (99.999%, Sigma-Aldrich, USA) at a mass fraction of 0.5 wt% for silica and 0.5 and 20 wt% for TEOS, respectively. The powder mixtures were ball-milled, spray-dried and pelletized using dry uniaxial pressing followed by cold isostatic pressing to form compact green bodies. The pressed samples were calcined in air at 600ºC for an hour, sintered in vacuum (10^{-6} torr) at 1735°C for 16 h, and subsequently annealed in air at 1100ºC for 100 h. The amount of silica was measured at various stage during the process (identified by asterisks in figure 30) by sampling pellets after cold isostatic pressing, calcination and vacuum sintering.

6.2 Fabrication of calibration samples

In order to quantify the concentration of SiO_2, calibration samples were fabricated by mixing aluminum and yttrium oxide in stoichiometric ratio. Silica powder was added to obtain powder compacts with 0, 0.17, 0.64, 0.84 and 1.08 wt% SiO_2 respectively. The experimental error on the silica loading is 0.02% due to weighing uncertainties. These mixtures were homogenized in the presence of ethanol in an alumina mortar, dried and uniaxially pressed to form powder compacts. This protocol ensures that chemical matrix effects do not influence the quantification of silica [91].

6.3 LIBS system and experimental protocol

The LIBS experiments were carried out on a J200 Tandem LA-LIBS system (Applied Spectra Inc.). The laser ablation was performed using a 8 ns, 266 nm Q-switched Nd:YAG laser operated at a repetition rate of 10 Hz. The laser pulse energy received by the sample was 14.7 mJ over a spot size of 100 μm, a size much larger than the individual particles and crystallites of the powder compacts and ceramics. The plasma emission was analyzed with a Czerny–Turner spectrometer (Isoplane, Princeton Instrument) with a 3600 grooves/mm grating centered at 288 nm, equipped with an ICCD detector (PIMAX4, Princeton Instrument). The gate delay and width were found optimal at 0.8 and 3 μs, respectively. Hundred spectra were accumulated on a single location to improve the signal-to-noise ratio, and this acquisition was repeated, for each sample, over 12 different locations on a 4x3 spot grid over a 1.2x1 mm^2 area to average any possible sampling inhomogeneities during the ablation process (figure 31 (a)).

The shot-to-shot fluctuations of the LIBS signal collected from 12 spots on a sample with SiO_2 loading of 0.838 wt% is shown in figure 31 (b) .The grey area in the figure represents the variation in the signal and the solid red curve is the average spectrum.

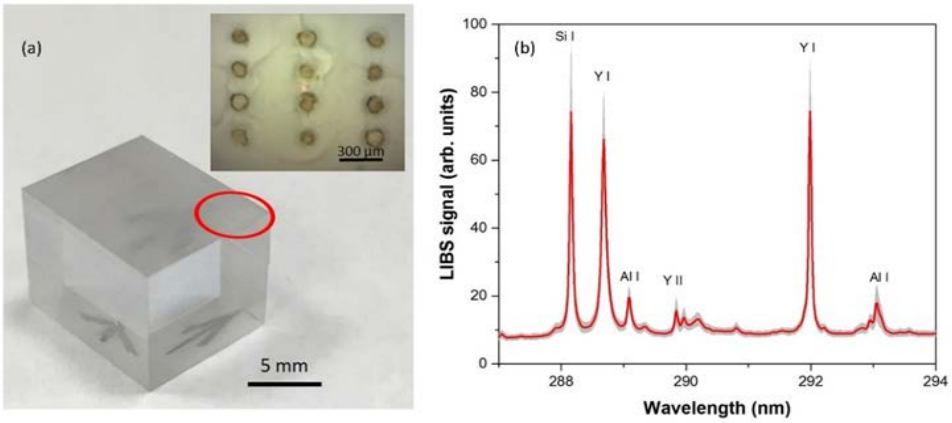


Figure 31. **(a)** Picture of an optical ceramic sample analyzed in the study. The inset shows the ablation craters left after the LIBS analysis. **(b)** Representative emission spectrum of a YAG ceramic analyzed by LIBS. In this example, the concentration of silica is 0.838 wt.%. The grey area in the figure represents the 1-sigma standard deviation of the signal and the solid red curve is the average spectrum.

6.4 Results and discussion

Because of possible disparities in laser-to-sample coupling due to variations in sample density, it is expected that under identical ablation conditions, the temperature of the plasma vary and lead to quantification inconsistencies. This effect, however, can be minimized by using spectral lines of major matrix elements to normalize the analyte peak intensity. This normalization follows from Boltzmann's equation applied to these emitters, and writes, at a plasma temperature T [79]:

$$\frac{I_{i,\mathrm{E_m}}}{I_{j,E_n}} \propto \frac{N_i(T)Z_j(T)}{N_j(\mathrm{T})\,\mathrm{Z}_i(\mathrm{T})} e^{-\frac{E_m-E_n}{kT}} \tag{61}$$

where N_k is the concentration of plasma species k, with partition function Z_k, emitting spectral lines of intensity $I_{k,\mathrm{Ei}}$ from upper levels of energy E_i. Hence, the influence of the plasma temperature on the intensity ratio can be minimized by choosing emitting levels whose difference in energy is small compared to kT. The silicon content in the YAG samples was then measured using the integrated intensity ratio of neutral silicon (288.158 nm) and neutral yttrium (288.654 nm) lines. The close proximity of the upper energy levels for these two transitions (ΔE~0.6 eV), relative to assessed plasma temperatures (on the order of kT~1-2 eV), helps minimize matrix effects caused by difference in laser-sample interaction. Spectral emission lines were identified using the National Institute of Standard and Technology (NIST) database [83]. It should be noted that neither self-absorption nor interference effects with other elements present in the plasma were observed for the two lines used in this analysis.

The calibration curve was obtained using purposely made samples and is shown in figure 32. In this figure, the normalized peak area of the Si line, A_{Si}, is plotted and fitted against the concentration of SiO_2, W_{SiO2}, present in the YAG samples using a linear regression, $A_{Si} = m \cdot W_{SiO2}$. The relative standard deviation (RSD) of the emission intensities ranges from 4 to 9%. The limit of detection (LOD) for SiO_2 was found to be 61 ppm in weight following the definition $\mathrm{LOD}=3 \cdot \sigma_{blank}/m$, where σ_{blank} is the standard deviation of LIBS signal from blank sample. Using this calibration curve, the amount of SiO_2 was monitored during the entire fabrication process of transparent YAG ceramics made by reactive sintering (Table 1, figure 30). In a sample batch in which an initial amount of 0.5 wt% of TEOS was added to the powder mixture of raw oxides (i.e. an equivalent of 0.166 wt% of SiO_2), we find that the mass of SiO_2 is actually 24% lower than expected. This drop, well outside the error bars of the quantification model, can be attributed to

the reagent-limited hydrolysis of TEOS during ball-milling leading to the evaporation of any TEOS excess during spray-drying. A further decrease of 6% occurs during the calcination of the sample at 600°C in air, followed by a major loss of 60% in the sintered sample, totaling a cumulative loss of SiO_2 up to 71%. This last departure of silica results from the formation of volatile silicon suboxides, SiO_x (x<2), during vacuum sintering at temperature above 1600ºC [41].

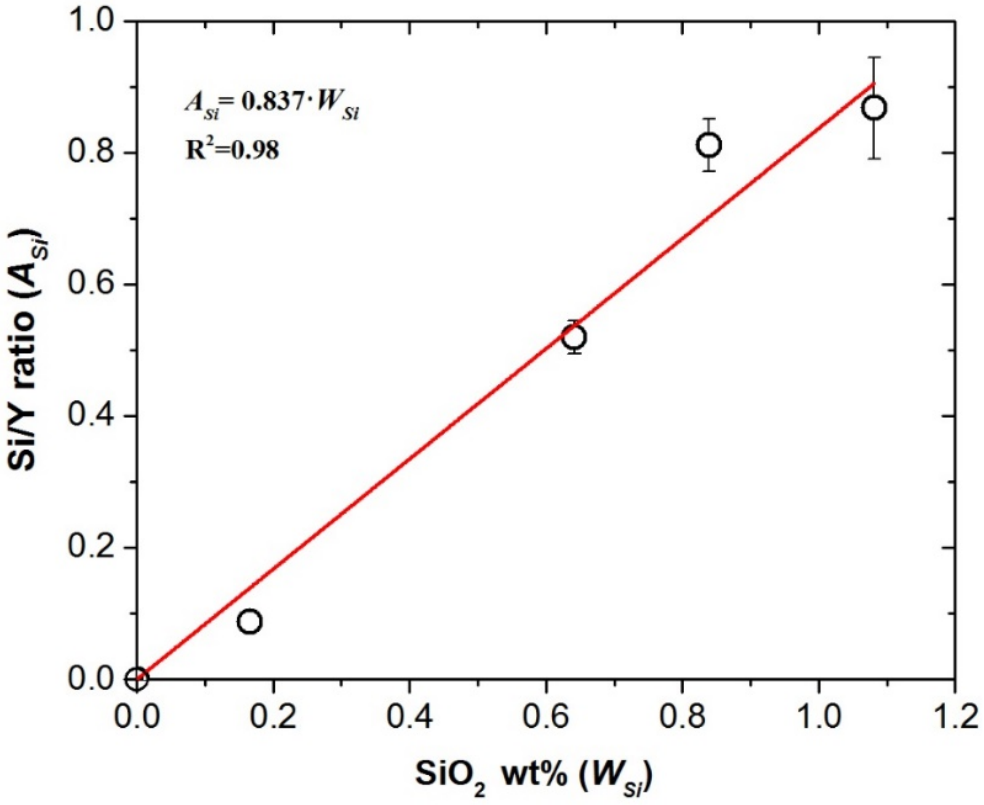


Figure 32. Calibration curve for the determination of SiO_2 concentration in YAG ceramics. The standard deviation of the blank sample is ±0.0017.

Table 1 Evolution of the concentration of SiO_2 during the fabrication of a transparent YAG ceramic sample made by reactive sintering of Y_2O_3 and Al_2O_3 powders and doped with 0.5wt% TEOS.

Ceramic sample state	**SiO_2 (wt.%)**	**Incremental loss of SiO_2 (%)**	**Cumulative loss of SiO_2 (%)**
Powder mixture before drying	0.145	0	0
Green body	0.111	24	24
Green body calcined at 600ºC	0.104	6	28
Sintered ceramic at 1735ºC	0.041	60	71

For comparison purposes only, a green body loaded with a large amount of TEOS (20 wt.%, an amount too large to produce transparent YAG ceramics) lost 98% of its silica content after firing, whereas a powder compact made with silica soot lost 88% after sintering. These results illustrate that the exact amount of silica loss varies greatly and depend on the fabrication protocol [10]. The figures above are only representative of the fact that large amounts of silica can be outgassed from the ceramic during extended firing, and that, in such open systems, the amount of silica participating to the densification of YAG is a hard figure to control.

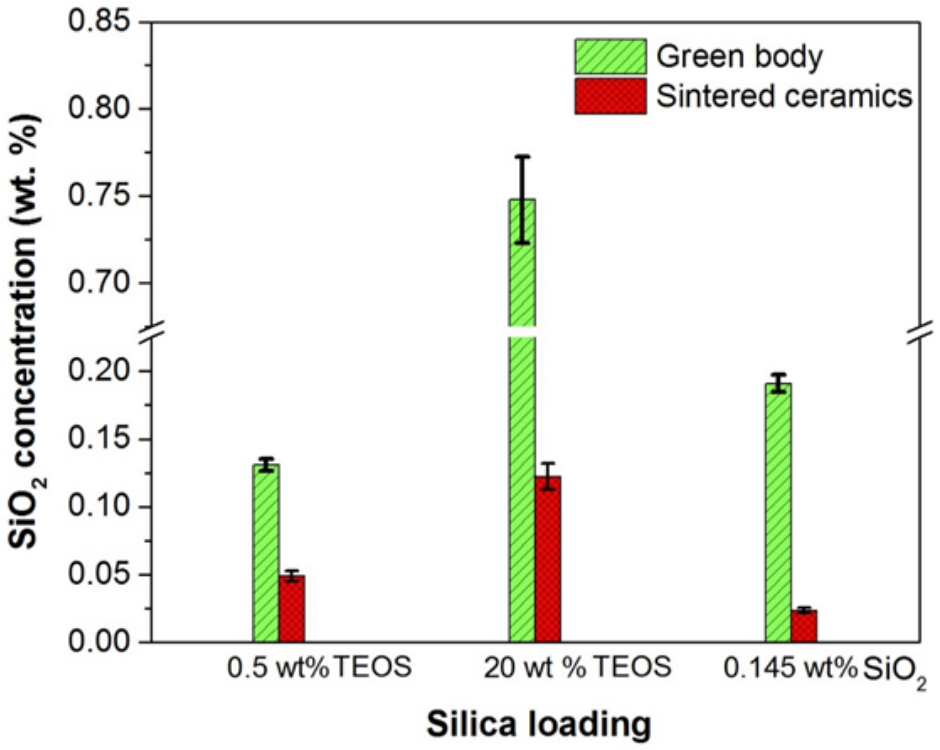


Figure 33. Evolution of the SiO_2 content in green bodies and sintered ceramics of YAG for different initial amounts of silica precursors.

6.5 Conclusion

This work details the protocol for the analysis of silica sintering additive in YAG ceramics by the LIBS technique. It shows that LIBS can be used to monitor the evolution of silica throughout the ceramic fabrication process from powdery samples, powder compacts, and fully-sintered transparent ceramics. The quantification of silica was accomplished using a calibration curve and the present limit of detection of our system amounts to 61ppm. Our results show that the large amounts of silica evaporated during the vacuum sintering of YAG ceramics at high temperatures can be monitored easily by LIBS and that this loss may help reduce the impact of this additive on the optical performance of YAG laser ceramics. We believe that this technique and similar

protocols will help better understand the role of sintering additives and control their effects in the processing of advanced ceramics.

CHAPTER SEVEN: CONCLUSION & PROSPECTS

The last seventy years have seen tremendous progress in the quality, material diversity, processes, functionalities and applications of transparent ceramics. From Coble's heroic experiments in the 1960s, transforming ceramic-ware looking alumina into see-through bodies, to the not least heroic >100 kW of CW power in a solid-state Nd:YAG ceramic laser obtained at Northrop-Grumman in 2007, transparent ceramics have transformed our common perception of what these polycrystalline materials enable. Yet, despite these fantastic advances and limited commercial deployments, the fabrication of high optical quality ceramics remains challenging in many respects, with specificities that distinguishes their preparation from that of their single-crystalline counterparts. This applies, for example, to the control of stoichiometry in multinary phases and to their densification from the powder state, so as to avoid the formation of deleterious scattering centers in the final part.

This thesis work introduces for the first time the notion that such problems can be addressed with more adequate analytical tools, allowing for enhanced sensitivity, precision and accuracy on the ratio of reactants before the synthesis of the ceramic phase. Specifically, we have shown that, contrary to other standard analytical techniques, laser-induced breakdown spectroscopy (LIBS) can be used effectively to quantify both stoichiometry shift and sintering additive concentration in YAG ceramics.

Our approach was fourfold: first, using simulations (Chapter 3), we evaluated the sensitivity of the atomic emission intensity ratio of aluminum and yttrium species to the LIBS plasma temperature. This helped us define the conditions for improved sensitivity for LIBS

measurements on YAG, estimate the limitations of the technique, and outline an experimental protocol for our quantification.

Then, we performed LIBS measurements on a set of yttrium aluminum oxide ceramics with Al/Y molar ratio ranging from 1.60 to 1.684 by 0.007 step-size increments (the ratio of 1.667 corresponding to the YAG composition). Following the results of our modeling, the laser irradiance was kept around 10^{13} $Wcm^{-2}s^{-1}$, a value which has been documented to yield plasma temperature in excess of 10000 K on solid targets. The intensity ratio of non-resonant spectral lines of singly-ionized aluminum (281.61 nm) and yttrium (278.52 nm) showed a positive correlation with their molar ratios. The standard deviation on the LIBS signal was less than 1% and sufficient to resolve stoichiometry shifts of 0.3 mol%.

Third, we tested the possibility of extending these results on powders and powder compacts (Chapter 5) so that this analysis could be done at the early stages of fabrication, while composition adjustments are still possible. This concept was tested by building a calibration curve using 200 nm, 500 nm and 30 μm alumina powders spiked with nickel at 500 to 3000 ppm concentration. LIBS experiments were performed on all three powder types with different degree of compaction, ranging from loose powders to 46% of full density. It was observed that a stable LIBS signal can only be achieved after the powders are compacted to more than 40% relative density, and that the error in the sensitivity of the calibration curve is reduced to 15% by this procedure. However, the excitation temperature was unaffected by the powder particle size and density of the powder compact. Sample particle size also affects the sensitivity. Two hundred nanometers and 500 nm ultimate particle sized samples have the same sensitivity and relative standard deviation at similar densities but the value for 30 μm powders were twice as high. The large shot-to-shot fluctuation

in powder compact implies that the LIBS measurement to determine stoichiometric shift may not be as sensitive as for sintered pellets.

Finally, we showed that our LIBS protocol could be extended to follow the concentration of SiO_2 sintering additive at different stages of the ceramic fabrication process (Chapter 6). Samples were taken right after cold pressing, calcination and sintering and measured against a purposely-made calibration curve with 61 ppm sensitivity. Our measurements showed that 24% of the initial SiO_2 doping was lost after powder drying, 28% after calcination at 600°C and 71% after sintering at 1750°C. Hence, the amount of silica that actually assist sintering is far less than the original amount and this may help better understand the kinetics and the role played by silica in the sintering YAG. In addition, this may provide a useful means to optimize the removal of silica after sintering, and reduce the color-centers it produces.

In summary, this work not only extends the range of capabilities of LIBS by showing how highly sensitive quantification on major elements can be performed in insulating materials, but also provides a new set of tools for quantifying narrow solid-state solutions in advanced materials and understanding the densification of ceramics. We foresee that such capability will be invaluable for quality control purposes, and in areas where fine and reproducible compositional tuning (defect engineering) is needed.

APPENDIX A: QUANTIFICATION OF NONSTOICHIOMETRY IN YAG BY ICP-AES

This appendix presents an attempt to measure the nonstoichiometry in YAG samples by inductively coupled plasma-atomic emission spectroscopy (ICP-AES). This mature and well established technique is routinely used for major, minor and trace elemental analysis [115]. In this technique, the sample is first completely dissolved in an appropriate solvent and then introduced into an inductively-coupled argon plasma through a nebulizer. It requires an extensive sample preparation but the matrix effect is avoided.

Eight of the YAG samples used in chapter four were chosen for the analysis[8]. Each of the samples was grounded for 30 minutes and fused with lithium metaborate ($LiBO_2$). The fused mixture was then dissolved in nitric acid according to protocol NF EN 725-1 and introduced into the plasma. The intensity ratio of Al/Y as a function of molar ratio is shown in figure 34. The relative standard deviation is 10%, an order of magnitude larger than in LIBS measurements. No apparent trend is observed between intensity and molar ratios.

[8] The experiment was performed in CRITT Matériaux Alsace (France) by Dr. Frédéric Pelascini.

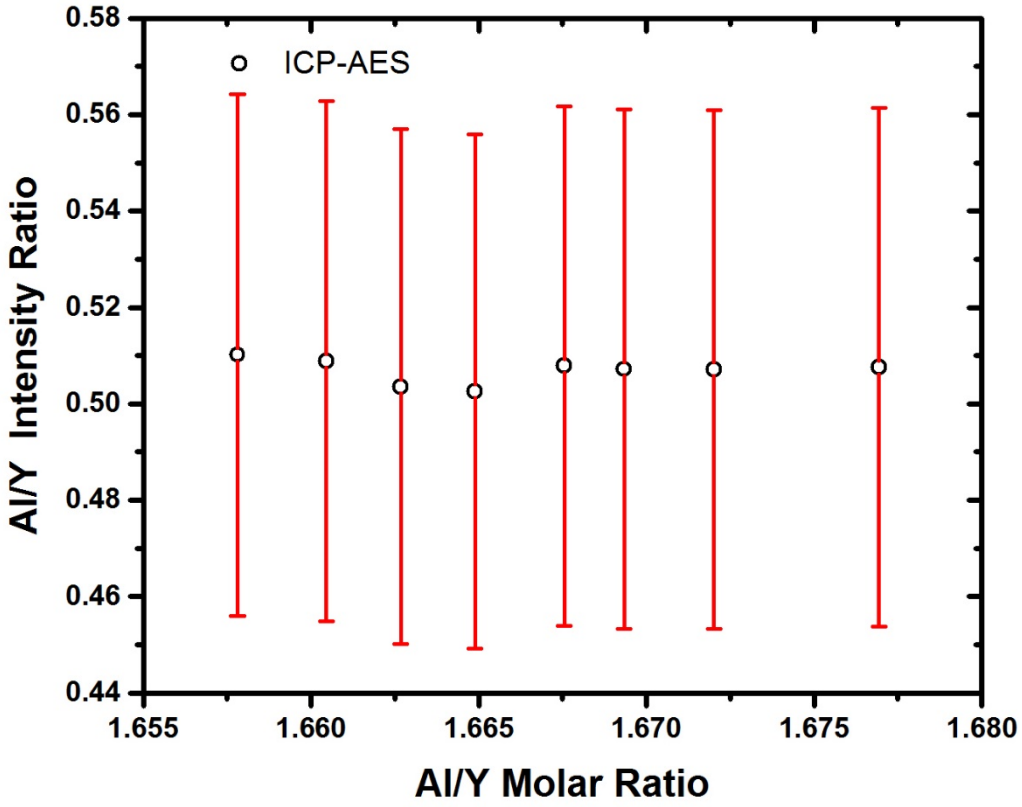


Figure 34. ICP-AES data of YAG samples with Al/Y ratio ranging from 1.657 to 1.667. No apparent relationship between intensity and molar ratios are observed. The relative standard deviation of measurements is 10%.

APPENDIX B: PUBLICATIONS

B.1 Journal publications

Pandey, S. J., Martinez, M., Pelascini, F., Motto-Ros, V., Baudelet, M., & Gaume, R. M. (2017). Quantification of non-stoichiometry in YAG ceramics using laser-induced breakdown spectroscopy. *Optical Materials Express*, *7*(2), 627-632.

Pandey, S. J., Martinez, M., Hostaša, J., Esposito, L., Baudelet, M., & Gaume, R. M. (2017). Quantification of SiO_2 Sintering Additive in YAG Transparent Ceramics by Laser-Induced Breakdown Spectroscopy (LIBS). *Optical Materials Express*, 7(5), 1666-1671.

Pandey, S. J., Locke, R., Gaume, R.M and Baudelet, M. Effect of powder compact density on the quantification of minor elements by LIBS. *Spectrochimica Acta B*, submitted.

Pandey, S. J., Joshi, G., Wang, S., Curtarolo, S., & Gaume, R. M. (2016). Modeling the Thermoelectric Properties of Ti_5O_9 Magnéli Phase Ceramics. Journal of Electronic Materials, 45(11), 5526-5532.

B.2 Conferences

Pandey, S., Shoulders, T., Wang, S., Curtarolo, S., & Gaume, R.M. Thermoelectric Characterization of Fine Grained Ti_5O_9 Magnéli Phase Ceramics, MS&T 2014, Pittsburgh, Pennsylvania.

Pandey, S.J., Locke, R., Martinez, M., Gaume, R.M., & Baudelet, M. Study of Matrix Effects for Reproducible LIBS analysis of Powders. SCIX 2016, Minnesota, Minneapolis.

LIST OF REFERENCES

1. Burke, J.E., *Lucalox alumina: The ceramic that revolutionized outdoor lighting.* MRS Bulletin, 1996. **21**(06): p. 61-68.

2. Krell, A., J. Klimke, and T. Hutzler, *Advanced spinel and sub-µm Al 2 O 3 for transparent armour applications.* Journal of the European Ceramic Society, 2009. **29**(2): p. 275-281.

3. Parish, M.V., M.R. Pascucci, and W.H. Rhodes. *Aerodynamic IR domes of polycrystalline alumina*. in *Defense and Security*. 2005. International Society for Optics and Photonics.

4. Haertling, G.H. and C.E. LAND, *Hot-Pressed (Pb, La)(Zr, Ti) O3 Ferroelectric Ceramics for Electrooptic Applications.* Journal of the American Ceramic Society, 1971. **54**(1): p. 1-11.

5. Wei, N., et al., *Transparent Ce: Y3Al5O12 ceramic phosphors for white light-emitting diodes.* Applied Physics Letters, 2012. **101**(6): p. 061902.

6. Greskovich, C. and S. Duclos, *Ceramic scintillators.* Annual review of materials science, 1997. **27**(1): p. 69-88.

7. Shoulders, W., *Barium Based Halide Scintillator Ceramics For Gamma Ray Detection.* 2013.

8. Ikesue, A., *Polycrystalline Nd: YAG ceramics lasers.* Optical materials, 2002. **19**(1): p. 183-187.

9. Chenais, S., et al., *Thermal lensing measurements in diode-pumped Yb-doped GdCOB, YCOB, YSO, YAG and KGW.* Optical materials, 2003. **22**(2): p. 129-137.

10. Lupei, V., et al., *Highly efficient 1063-nm continuous-wave laser emission in Nd: GdVO 4.* Optics letters, 2003. **28**(23): p. 2366-2368.

11. Goldstein, A. and A. Krell, *Transparent Ceramics at 50: Progress Made and Further Prospects.* Journal of the American Ceramic Society, 2016.

12. Ikesue, A., I. Furusato, and K. Kamata, *Fabrication of Polycrystal line, Transparent YAG Ceramics by a Solid-State Reaction Method.* Journal of the American Ceramic Society, 1995. **78**(1): p. 225-228.

13. Li, Z., et al., *Mechanism of Intrinsic Point Defects and Oxygen Diffusion in Yttrium Aluminum Garnet: First-Principles Investigation.* Journal of the American Ceramic Society, 2012. **95**(11): p. 3628-3633.

14. Shikao, S. and W. Jiye, *Combustion synthesis of Eu 3+ activated Y 3 Al 5 O 12 phosphor nanoparticles.* Journal of alloys and compounds, 2001. **327**(1): p. 82-86.

15. Zhu, L.-L., et al., *Preparation and characterization of non-stoichiometric yttrium aluminum garnet (YAG) with antisite defects as a potential scintillator.* Nuclear Science, IEEE Transactions on, 2014. **61**(1): p. 312-315.

16. Nishiura, S., et al., *Properties of transparent Ce: YAG ceramic phosphors for white LED.* Optical Materials, 2011. **33**(5): p. 688-691.

17. Qin, H., et al., *Effect of composition deviation on the microstructure and luminescence properties of Nd:YAG ceramics.* CrystEngComm, 2014. **16**(47): p. 10856-10862.

18. Matsushita, N., et al., *Precipitation and calcination processes for yttrium aluminum garnet precursors synthesized by the urea method.* Journal of the American Ceramic Society, 1999. **82**(8): p. 1977-1984.

19. Van Dijk, H., *Translucent Y3Al5O12 ceramics.* Materials research bulletin, 1984. **19**(12): p. 1669-1674.

20. Li, J.G., et al., *Low-Temperature Fabrication of Transparent Yttrium Aluminum Garnet (YAG) Ceramics without Additives.* Journal of the American Ceramic Society, 2000. **83**(4): p. 961-963.

21. Ikesue, A., et al., *Optical scattering centers in polycrystalline Nd: YAG laser.* Journal of the American Ceramic Society, 1997. **80**(6): p. 1517-1522.

22. Boulesteix, R. 2017.

23. Lee, S.H., et al., *Solid-State Reactive Sintering of Transparent Polycrystalline Nd: YAG Ceramics.* Journal of the American Ceramic Society, 2006. **89**(6): p. 1945-1950.

24. Kinsman, K.M., et al., *Phase development and luminescence in chromium-doped yttrium aluminum garnet (YAG: Cr) phosphors.* Journal of the American Ceramic Society, 1994. **77**(11): p. 2866-2872.

25. Rahaman, M.N., *Ceramic Processing*. 2006: Taylor & Francis. 1-98.

26. Stevenson, A.J., et al., *Effect of SiO_2 on densification and microstructure development in Nd:YAG transparent ceramics.* Journal of the American Ceramic Society, 2011. **94**(5): p. 1380-1387.

27. Patel, A., et al., *Mechanisms of nonstoichiometry in Y3Al5O12.* Applied Physics Letters, 2008. **93**(19): p. 191902.

28. Kuklja, M.M., *Defects in yttrium aluminium perovskite and garnet crystals: atomistic study.* Journal of Physics: Condensed Matter, 2000. **12**(13): p. 2953.

29. Nikl, M., *Scintillation detectors for x-rays.* Measurement Science and Technology, 2006. **17**(4): p. R37.

30. Ikesue, A. and K. Yoshida, *Influence of pore volume on laser performance of Nd: YAG ceramics.* Journal of materials science, 1999. **34**(6): p. 1189-1195.

31. Boulesteix, R., et al., *Light scattering by pores in transparent Nd: YAG ceramics for lasers: correlations between microstructure and optical properties.* Optics express, 2010. **18**(14): p. 14992-15002.

32. Liu, W., et al., *2.44 KW laser output of Nd: YAG ceramic slab fabricated by a solid-state reactive sintering.* Journal of Alloys and Compounds, 2012. **538**: p. 258-261.

33. Goodno, G., et al. *Multi-kW near-diffraction-limited single-frequency Nd: YAG laser*. in *Lasers and Electro-Optics Europe, 2005. CLEO/Europe. 2005 Conference on*. 2005. IEEE.

34. Ikesue, A., et al., *Optical Scattering Centers in Polycrystalline Nd:YAG Laser.* Journal of the American Ceramic Society, 2005. **80**(6): p. 1517-1522.

35. Kochawattana, S., et al., *Sintering and grain growth in SiO_2 doped Nd:YAG.* Journal of the European Ceramic Society, 2008. **28**(7): p. 1527-1534.

36. De With, G. and J. Parren, *Translucent Y3Al5O12 ceramics: mechanical properties.* Solid State Ionics, 1985. **16**: p. 87-93.

37. Boulesteix, R., et al., *Mechanism of the liquid-phase sintering for Nd: YAG ceramics.* Optical Materials, 2009. **31**(5): p. 711-715.

38. Jiménez-Melendo, M., H. Haneda, and H. Nozawa, *Ytterbium cation diffusion in yttrium aluminum garnet (YAG)—implications for creep mechanisms.* Journal of the American Ceramic Society, 2001. **84**(10): p. 2356-2360.

39. Gaume, R., et al., *Effect of Si-induced defects on 1 um absorption losses in laser-grade YAG ceramics.* Journal of Applied Physics, 2012. **111**(9): p. 093104.

40. Fagundes-Peters, D., et al., *High quantum efficiency YbAG-crystals.* Journal of luminescence, 2007. **125**(1): p. 238-247.

41. Gaume, R., et al., *Effect of Si-induced defects on 1 μm absorption losses in laser-grade YAG ceramics.* Journal of Applied Physics, 2012. **111**(9): p. 093104.

42. Cremers, D.A., et al., *Laser-Induced Breakdown Spectroscopy, Elemental Analysis.* Encyclopedia of Analytical Chemistry, 2006.

43. Hahn, D.W. and N. Omenetto, *Laser-induced breakdown spectroscopy (LIBS), part II: review of instrumental and methodological approaches to material analysis and applications to different fields.* Applied spectroscopy, 2012. **66**(4): p. 347-419.

44. Michel, A.P.M., *Review: Applications of single-shot laser-induced breakdown spectroscopy.* Spectrochimica Acta Part B: Atomic Spectroscopy, 2010. **65**(3): p. 185-191.

45. Naes, B.E., et al., *A comparison of laser ablation inductively coupled plasma mass spectrometry, micro X-ray fluorescence spectroscopy, and laser induced breakdown spectroscopy for the discrimination of automotive glass.* Spectrochimica Acta Part B: Atomic Spectroscopy, 2008. **63**(10): p. 1145-1150.

46. Harmon, R.S., R.E. Russo, and R.R. Hark, *Applications of laser-induced breakdown spectroscopy for geochemical and environmental analysis: A comprehensive review.* Spectrochimica Acta Part B: Atomic Spectroscopy, 2013. **87**: p. 11-26.

47. Ismaël, A., et al., *In situ semi-quantitative analysis of polluted soils by laser-induced breakdown spectroscopy (LIBS).* Applied spectroscopy, 2011. **65**(5): p. 467-473.

48. Gruber, J., et al., *Rapid in-situ analysis of liquid steel by laser-induced breakdown spectroscopy.* Spectrochimica Acta Part B: Atomic Spectroscopy, 2001. **56**(6): p. 685-693.

49. Noll, R., et al., *Laser-induced breakdown spectroscopy expands into industrial applications.* Spectrochimica Acta Part B: Atomic Spectroscopy, 2014. **93**: p. 41-51.

50. Pandey, S.J., et al., *Quantification of non-stoichiometry in YAG ceramics using laser-induced breakdown spectroscopy.* Optical Materials Express, 2017. **7**(2): p. 627-632.

51. Pandey, S.J., et al., *Quantification of SiO2 sintering additive in YAG transparent ceramics by laser-induced breakdown spectroscopy (LIBS).* Optical Materials Express, 2017. **7**(5): p. 1666-1671.

52. Hilbk-Kortenbruck, F., et al., *Analysis of heavy metals in soils using laser-induced breakdown spectrometry combined with laser-induced fluorescence.* Spectrochimica Acta Part B: Atomic Spectroscopy, 2001. **56**(6): p. 933-945.

53. Sirven, J.-B., et al., *Qualitative and quantitative investigation of chromium-polluted soils by laser-induced breakdown spectroscopy combined with neural networks analysis.* Analytical and bioanalytical chemistry, 2006. **385**(2): p. 256-262.

54. Dell'Aglio, M., et al., *Monitoring of Cr, Cu, Pb, V and Zn in polluted soils by laser induced breakdown spectroscopy (LIBS).* Journal of Environmental Monitoring, 2011. **13**(5): p. 1422-1426.

55. El Haddad, J., et al., *Application of a series of artificial neural networks to on-site quantitative analysis of lead into real soil samples by laser induced breakdown spectroscopy.* Spectrochimica Acta Part B: Atomic Spectroscopy, 2014. **97**: p. 57-64.

56. Anderson, R.B., et al., *The influence of multivariate analysis methods and target grain size on the accuracy of remote quantitative chemical analysis of rocks using laser induced breakdown spectroscopy.* Icarus, 2011. **215**(2): p. 608-627.

57. Lazic, V., et al., *Laser induced breakdown spectroscopy of soils, rocks and ice at subzero temperatures in simulated martian conditions.* Spectrochimica Acta Part B: Atomic Spectroscopy, 2007. **62**(12): p. 1546-1556.

58. Cremers, D.A., *Space applications of LIBS*, in *Laser-Induced Breakdown Spectroscopy*. 2014, Springer. p. 257-291.

59. Baudelet, M., et al., *Femtosecond time-resolved laser-induced breakdown spectroscopy for detection and identification of bacteria: A comparison to the nanosecond regime.* Journal of Applied Physics, 2006. **99**(8): p. 084701.

60. Baudelet, M., et al., *Discrimination of microbiological samples using femtosecond laser-induced breakdown spectroscopy.* Applied physics letters, 2006. **89**(16): p. 163903.

61. Jantzi, S.C. and J.R. Almirall, *Characterization and forensic analysis of soil samples using laser-induced breakdown spectroscopy (LIBS).* Analytical and bioanalytical chemistry, 2011. **400**(10): p. 3341-3351.

62. Martin, M.Z., et al., *High resolution applications of laser-induced breakdown spectroscopy for environmental and forensic applications.* Spectrochimica Acta Part B: Atomic Spectroscopy, 2007. **62**(12): p. 1426-1432.

63. Bridge, C.M., et al., *Forensic comparative glass analysis by laser-induced breakdown spectroscopy.* Spectrochimica Acta Part B: Atomic Spectroscopy, 2007. **62**(12): p. 1419-1425.

64. Tarifa, A. and J.R. Almirall, *Fast detection and characterization of organic and inorganic gunshot residues on the hands of suspects by CMV-GC–MS and LIBS.* Science & Justice, 2015. **55**(3): p. 168-175.

65. Popescu, A.C., et al., *Analysis of indium zinc oxide thin films by laser-induced breakdown spectroscopy.* Journal of Applied Physics, 2011. **110**(8): p. 083116.

66. Caneve, L., et al., *Laser-induced breakdown spectroscopy as a diagnostic tool for thin films elemental composition.* Spectrochimica Acta Part B: Atomic Spectroscopy, 2005. **60**(7-8): p. 1098-1102.

67. Aragón, C., V. Madurga, and J.A. Aguilera, *Application of laser-induced breakdown spectroscopy to the analysis of the composition of thin films produced by pulsed laser deposition.* Applied Surface Science, 2002. **197-198**: p. 217-223.

68. Acquaviva, S., et al., *Laser-induced breakdown spectroscopy for compositional analysis of multielemental thin films.* Spectrochimica Acta Part B: Atomic Spectroscopy, 2006. **61**(7): p. 810-816.

69. Noll, R., *Laser-induced breakdown spectroscopy*, in *Laser-Induced Breakdown Spectroscopy*. 2012, Springer. p. 7-15.

70. Aguilera, J. and C. Aragón, *Multi-element Saha–Boltzmann and Boltzmann plots in laser-induced plasmas.* Spectrochimica Acta Part B: Atomic Spectroscopy, 2007. **62**(4): p. 378-385.

71. Hahn, D.W. and N. Omenetto, *Laser-induced breakdown spectroscopy (LIBS), part I: review of basic diagnostics and plasma–particle interactions: still-challenging issues within the analytical plasma community.* Applied spectroscopy, 2010. **64**(12): p. 335A-366A.

72. Eliezer, S., et al., *An introduction to equations of state: theory and applications.* An introduction to equations of state: theory and applications.. S. Eliezer, A. Ghatak, H. Hora, with a foreword by E. Teller. Cambridge University Press, Cambridge-London-New York-New Rochelle-Melbourne-Sydney. 12+ 366 pp. Price£ 45.00, US $69.50 (1986). ISBN 0-521-30389-3., 1986.

73. Hollas, J.M., *Modern spectroscopy*. 2004: John Wiley & Sons.

74. Griem, H.R., *Principles of plasma spectroscopy*. Vol. 2. 2005: Cambridge University Press.

75. Walsh, A., *The application of atomic absorption spectra to chemical analysis.* Spectrochimica Acta, 1955. **7**: p. 108-117.

76. Bekefi, G., *Principles of laser plasmas.* New York, Wiley-Interscience, 1976. 712 p, 1976.

77. Olivero, J.J. and R. Longbothum, *Empirical fits to the Voigt line width: A brief review.* Journal of Quantitative Spectroscopy and Radiative Transfer, 1977. **17**(2): p. 233-236.

78. Thorne, A., U. Litzén, and S. Johansson, *Spectrophysics: principles and applications*. 1999: Springer Science & Business Media.

79. Noll, R., *Laser-induced breakdown spectroscopy*. Laser-Induced Breakdown Spectroscopy. 2012: Springer. 7-15.

80. Wood, R.M., *Laser damage in optical materials*. 1986: Adam Hilger.

81. Fassel, V.A., *Quantitative Elemental Analyses by Plasma Emission Spectroscopy.* Science, 1978. **202**(4364): p. 183-191.

82. Self, S.A., *Focusing of spherical Gaussian beams.* Applied optics, 1983. **22**(5): p. 658-661.

83. Kramida, A., Ralchenko, Yu., Reader, J. and NIST ASD Team *NIST Atomic Spectra Database* 2016 [cited 2016 Dec 13]; version 5.4:[Available from: http://physics.nist.gov/asd.

84. Ashrafkhani, B., M. Bahreini, and S.H. Tavassoli, *Repeatability improvement of laser-induced breakdown spectroscopy using an auto-focus system.* Optics and Spectroscopy, 2015. **118**(5): p. 841-846.

85. Motto-Ros, V., et al., *Precise alignment of the collection fiber assisted by real-time plasma imaging in laser-induced breakdown spectroscopy.* Spectrochimica Acta Part B: Atomic Spectroscopy, 2014. **92**: p. 60-69.

86. Kazemi, A.J., *Highly-sensitive stoichiometric analysis of yag ceramics using laser-induced breakdown spectroscopy (libs)*, in *College of Optics and Photonics*. 2014, Univeristy of Central Florida: Orlando, FL.

87. Negre, E., et al., *On the performance of laser-induced breakdown spectroscopy for quantitative analysis of minor and trace elements in glass.* Journal of Analytical Atomic Spectrometry, 2015. **30**(2): p. 417-425.

88. Effenberger, A.J. and J.R. Scott, *Effect of atmospheric conditions on LIBS spectra.* Sensors, 2010. **10**(5): p. 4907-4925.

89. Aguilera, J., J. Bengoechea, and C. Aragon, *Spatial characterization of laser induced plasmas obtained in air and argon with different laser focusing distances.* Spectrochimica Acta Part B: Atomic Spectroscopy, 2004. **59**(4): p. 461-469.

90. Iida, Y., *Effects of atmosphere on laser vaporization and excitation processes of solid samples.* Spectrochimica Acta Part B: Atomic Spectroscopy, 1990. **45**(12): p. 1353-1367.

91. Eppler, A.S., et al., *Matrix effects in the detection of Pb and Ba in soils using laser-induced breakdown spectroscopy.* Applied Spectroscopy, 1996. **50**(9): p. 1175-1181.

92. Wisburn, R., et al., *Detector for trace elemental analysis of solid environmental samples by laser plasma spectroscopy.* Analytical Chemistry, 1994. **66**(18): p. 2964-2975.

93. S.J.Pandey, et al., *Quantification of non-stoichiometry in YAG ceramics using laser-induced breakdown spectroscopy*. 2017: Optical Material Express.

94. Simmons, J.D. and J.K. McDonald, *The emission spectrum of AlN.* Journal of Molecular Spectroscopy, 1972. **41**(3): p. 584-594.

95. Coccia, L.G., G.C. Tyrrell, and I.W. Boyd, *Gas-phase reactions during reactive laser ablation of Ti and Si in N2 and O2 rarefied atmospheres analysed using energy-dispersive mass spectrometry.* Applied Surface Science, 1997. **109-110**: p. 413-418.

96. Olsen, H.N., *Partition Function Cutoff and Lowering of the Ionization Potential in an Argon Plasma.* Physical Review, 1961. **124**(6): p. 1703-1708.

97. Zeldovich, Y.B. and Y.P. Raizer, *Physics of shock waves and high-temperature hydrodynamic phenomena*. 1965, FOREIGN TECHNOLOGY DIV WRIGHT-PATTERSON AFB OH.

98. Linstrom, P. and W. Mallard, *NIST chemistry webbook, NIST standard reference database number 69, National Institute of Standards and Technology, Gaithersburg MD, 20899*. 2010.

99. Hermann, J. and C. Dutouquet, *Local thermal equilibrium plasma modeling for analyses of gas-phase reactions during reactive-laser ablation.* Journal of applied physics, 2002. **91**(12): p. 10188-10193.

100. Kurucz, R.L. *The Kurucz Smithsonian atomic and molecular database*. in *Astrophysical Applications of Powerful New Databases*. 1995.

101. Cowan, R.D. and G.H. Dieke, *Self-Absorption of Spectrum Lines.* Reviews of Modern Physics, 1948. **20**(2): p. 418-455.

102. Aragón, C. and J.A. Aguilera, *Characterization of laser induced plasmas by optical emission spectroscopy: A review of experiments and methods.* Spectrochimica Acta Part B: Atomic Spectroscopy, 2008. **63**(9): p. 893-916.

103. Radziemski, L.J. and D.A. Cremers, *Handbook of Laser Induced Breakdown Spectroscopy*. 2006, John Wiley & Sons, West Sussex, England.

104. Prahl, S. *Mie Scattering Calculator, http://omlc.org/calc/mie_calc.html*. 2017 [cited 2017 5/1/2017]; Available from: http://omlc.org/calc/mie_calc.html.

105. Kramida, A., Ralchenko, Yu., Reader, J. and NIST ASD Team *NIST Atomic Spectra Database, http://physics.nist.gov/asd*. 2016 [cited 2016 Dec 13]; version 5.4:[Available from: http://physics.nist.gov/asd.

106. Sivakumar, P., et al., *Packing density effects on the fluctuations of the emission lines in laser-induced breakdown spectroscopy.* Spectrochimica Acta Part B: Atomic Spectroscopy, 2014. **92**: p. 84-89.

107. Hübner, S. and A. Melzer, *Dust-induced modulation of the atomic emission in a dusty argon discharge.* Physical review letters, 2009. **102**(21): p. 215001.

108. Ratynskaia, S., et al., *Observation of the effects of dust particles on plasma fluctuation spectra.* Physical review letters, 2007. **99**(7): p. 075002.

109. Bousquet, B., J.-B. Sirven, and L. Canioni, *Towards quantitative laser-induced breakdown spectroscopy analysis of soil samples.* Spectrochimica Acta Part B: Atomic Spectroscopy, 2007. **62**(12): p. 1582-1589.

110. Rauschenbach, I., et al., *Laser induced breakdown spectroscopy on soils and rocks: Influence of the sample temperature, moisture and roughness.* Spectrochimica Acta Part B: Atomic Spectroscopy, 2008. **63**(10): p. 1205-1215.

111. Jantzi, S.C. and J.R. Almirall, *Elemental Analysis of Soils Using Laser Ablation Inductively Coupled Plasma Mass Spectrometry (LA-ICP-MS) and Laser-Induced Breakdown Spectroscopy (LIBS) with Multivariate Discrimination: Tape Mounting as an Alternative to Pellets for Small Forensic Transfer Specimens.* Applied Spectroscopy, 2014. **68**(9): p. 963-974.

112. El Haddad, J., et al., *Artificial neural network for on-site quantitative analysis of soils using laser induced breakdown spectroscopy.* Spectrochimica Acta Part B: Atomic Spectroscopy, 2013. **79**: p. 51-57.

113. Cisewski, J., et al., *Support vector machine classification of suspect powders using laser-induced breakdown spectroscopy (LIBS) spectral data.* Journal of Chemometrics, 2012. **26**(5): p. 143-149.

114. Dingari, N.C., et al., *Incorporation of Support Vector Machines in the LIBS Toolbox for Sensitive and Robust Classification Amidst Unexpected Sample and System Variability.* Analytical Chemistry, 2012. **84**(6): p. 2686-2694.

115. Bings, N.H., A. Bogaerts, and J.A.C. Broekaert, *Atomic Spectroscopy: A Review.* Analytical Chemistry, 2010. **82**(12): p. 4653-4681.